**ANKARA YILDIRIM BEYAZIT UNIVERSITY**

**GRADUATE SCHOOL OF NATURAL AND APPLIED SCIENCE**




# EFFECTS OF SUBSTRATES ON CHARACTERISTICS OF SNS THIN FILMS AND DEVICE APPLICATION ON SILICON

**M.Sc. Thesis by**

**Ceren YILDIRIM**

**Department of Energy Systems Engineering**

**August 2020**

**ANKARA**

# EFFECTS OF SUBSTRATES ON CHARACTERISTICS OF SNS THIN FILMS AND DEVICE APPLICATION ON SILICON

**A Thesis Submitted to**

**The Graduate School of Natural and Applied Sciences of**

**Ankara Yıldırım Beyazıt University**

**In Partial Fulfillment of the Requirements for the Degree of Master of Science in Energy Systems Engineering, Department of Energy Systems Engineering**

**by**

**Ceren YILDIRIM**

**August 2020**

**ANKARA**

## M.Sc. THESIS EXAMINATION RESULT FORM

We have read the thesis entitled **"EFFECTS OF SUBSTRATES ON CHARACTERISTICS OF SNS THIN FILMS AND DEVICE APPLICATION ON SILICON"** completed by **CEREN YILDIRIM** under the supervision of **PROF. DR. ABDULLAH YILDIZ** and we certify that in our opinion it is fully adequate, in scope and in quality, as a thesis for the degree of Master of Science.

Prof. Dr. Abdullah YILDIZ

Supervisor

Prof. Dr. Bülent YEŞİLATA

Jury Member

Prof. Dr. Sefer Bora LİŞESİVDİN

Jury Member

Assoc. Prof. Dr. Şinası Barış EMRE

Jury Member

Asst. Prof. Dr. Özge SÜRÜCÜ

Jury Member

Prof. Dr. Ergün ERASLAN

Director

Graduate School of Natural and Applied Sciences

# ETHICAL DECLARATION

I hereby declare that, in this thesis which has been prepared in accordance with the Thesis Writing Manual of Graduate School of Natural and Applied Sciences,

- All data, information and documents are obtained in the framework of academic and ethical rules,
- All information, documents and assessments are presented in accordance with scientific ethics and morals,
- All the materials that have been utilized are fully cited and referenced,
- No change has been made on the utilized materials,
- All the works presented are original,

and in any contrary case of above statements, I accept to renounce all my legal rights.

**Date: 31/08/2020** **Signature: ……..**

**Name & Surname: Ceren YILDIRIM**

# ACKNOWLEDGEMENTS

I would like to express my deepest gratitude to my supervisor Prof. Dr. Abdullah YILDIZ for allowing me to work in his research group. I will always be grateful to him for his intense interest, guidance and advice from the beginning of my master's program. I would also like to thank Asst. Prof. Dr. Hasan Hüseyin GÜLLÜ, who is my co-advisor, for patience and continuous support. I am grateful to him for his scientific advice and guidance throughout my thesis.

Besides, I would also to extend my gratitude to Middle East Technical University Physics Department where I conducted my thesis work, especially Prof. Dr. Mehmet PARLAK for opening his laboratory to me. I specially thank Asst. Prof. Dr. Özge SÜRÜCÜ and Dr. Makbule TERLEMEZOĞLU for their help and informative advice in this research.

I would also like to thank Yıldız Research Group for all kinds of support during my master program. I would like to thank the PhD. students Abdullah ATILGAN and Aycan ATLI who guided me on the right path.

I would like to express my sincere thanks to Aydan ÖZEL, who has always been special for me, her support and invaluable friendship. I also thank my dear friend Mücahit ÇAĞDAŞ for motivational speeches.

Last but not least, I thank my family, Ayşe-Mevlüt YILDIRIM, who has been my biggest supporter in my entire life, for their endless love. There is no word to explain gratitude to my family for being there at my every moment and for always believing in me. Thank you to my brother, Çağdaş YILDIRIM, for everything and also niece, Eliz YILDIRIM, who is our joy in life. Also, thank you to my cat, Pepe, who always kept my sense of compassion alive. I feel lucky to have all this.

**Tarih 31/08/2020** **Ceren YILDIRIM**

# EFFECTS OF SUBSTRATES ON CHARACTERISTICS OF SNS THIN FILMS AND DEVICE APPLICATION ON SILICON

## ABSTRACT

The aim of this thesis is to investigate the deposited on different substrates SnS thin films in terms of structural, surface and optical properties. In addition to these, the electrical properties of SnS thin film have been focused.

In this context, SnS thin films were first deposited on soda lime glass (SLG), silicon (Si), ITO and FTO substrates using electron-beam technique. Structural characterization of the films was done using X-ray diffraction (XRD) and energy dispersive spectrometry (EDS). It was used for surface analyze of the SnS thin films for atomic force microscopy (AFM) and scanning electron microscopy (SEM). UV-Vis spectroscopy was utilized for optical characterization of the films and band gap values were calculated. Electrical characterization of the SnS thin films was carried out via temperature-dependent current-voltage (I-V) and photoconductivity measurement. In the next step, device characterization of SnS/Si structure was performed. Likewise, electrical characterization was done for device performance. In addition, I-V measurement under dark and different light intensity conditions was carried out at room temperature.

According to the results, it was determined that the SnS thin films deposited on different substrates showed structural, surface and optical properties which correspond to the literature. It was also determined that the SnS/Si structure had photodiode behavior.

**Keywords:** SnS, thin film, electron-beam and photodiode

# ALTTAŞLARIN SNS İNCE FİLMLERİN ÖZELLİKLERİNİNE ETKİSİ VE SİLİKON ÜZERİNE CİHAZ UYGULAMASI

## ÖZ

Bu tezin amacı, farklı yüzeylerde biriktirilen SnS ince filmlerinin yapısal, yüzey ve optik özellikleri açısından incelenmesidir. Bunlara ek olarak SnS ince filmin elektriksel özelliklerine de odaklanılmıştır.

Bu bağlamda, SnS ince filmler ilk olarak elektron ışını tekniği kullanılarak soda kireç camı (SLG), silikon (Si), indiyum katkılı kalay oksit (ITO) ve flor katkılı kalay oksit (FTO) alttaşları üzerine büyütülmüştür. Filmlerin yapısal karakterizasyonu, X-ışını kırınımı (XRD) ve enerji dağıtıcı spektrometresi (EDS) kullanılarak yapıldı. Atomik kuvvet mikroskobu (AFM) ve taramalı elektron mikroskobu (SEM) SnS ince filmlerinin yüzey analizi için kullanıldı. Filmlerin optik karakterizasyonu için UV-Vis spektroskopisi kullanılmış ve bant aralığı değerleri hesaplanmıştır. SnS ince filmlerin elektriksel karakterizasyonu, sıcaklığa bağlı akım-voltaj (I-V) ve fotoiletkenlik ölçümü yoluyla gerçekleştirildi. Bir sonraki adımda SnS / Si yapısının cihaz karakterizasyonu gerçekleştirildi. Aynı şekilde, cihaz performansı için elektriksel karakterizasyon yapıldı. Ayrıca oda sıcaklığında karanlık ve farklı ışık yoğunluğu koşullarında I-V ölçümü gerçekleştirildi.

Elde edilen sonuçlara göre, farklı yüzeyler üzerine serilen SnS ince filmlerin literatüre karşılık gelen yapısal, yüzey ve optik özellikler gösterdiği tespit edildi. SnS / Si yapısının fotodiyot davranışı sağladığı da belirlendi.

**Anahtar kelimeler:** SnS, ince film, elektron-ışını ve fotodiyot

# NOMANCLATURE

## Symbols

| | |
|---|---|
| $E_a$ | Activation energy |
| $E_g$ | Energy of incident photon |
| $I_{sc}$ | Short circuit |
| $I_{ph}$ | Photocurrent |
| $I_0$ | Diode saturation current |
| $J_0$ | Reverse saturation current density |
| $J_{sc}$ | Short-circuits current density |
| k | Extinction coefficient |
| K | Scherer's constant |
| $k_B$ | Boltzmann's constant |
| L | Electron diffusion length |
| n | Refractive index |
| $n_i$ | Intrinsic carrier concentration |
| Q | Charge density |
| $R_L$ | External load resistance |
| $R_s$ | Series resistance |
| $R_{sh}$ | Shunt resistance |
| $V_b$ | Built-in voltage |
| $V_{oc}$ | Open circuit voltage |
| $\chi$ | Electron affinity |
| W | Depletion region width |
| $\upsilon_d$ | Drift velocity |
| $Ø_p$ | Incident photon flux |
| $\alpha$ | Absorption coefficient |
| $\varepsilon$ | Dielectric constant |
| $\sigma$ | Electrical conductivity |

| | |
|---|---|
| $\lambda$ | Incident wavelength of radiation |
| $\varphi$ | Spectral frequency |
| $\rho$ | Resistivity |
| $\tau$ | Recombination lifetime |
| $\phi$ | Work function |
| $\eta$ | Power conversion efficiency |
| $2\theta$ | Measured between the incident beams called as Bragg angle |
| $\Omega$ | Ohm |

**Acronyms**

| | |
|---|---|
| AFM | Atomic force microscopy |
| CIG | Copper-indium-gallium |
| CIGS | Copper-indium-gallium-selenide |
| EDS | Energy dispersive spectroscopy |
| FF | Fill factor |
| FWHM | Full width at half maximum |
| IR | Near-infrared |
| I-V | Current-voltage |
| PCE | Power conversion efficiency |
| PV | Photovoltaic |
| PVD | Physical vapor deposition |
| RMS | Root mean square |
| SEM | Scanning electron microscopy |
| TCO | Transparent conductive oxide |
| TE | Thermionic emission |
| UV-Vis | Ultraviolet-visible |
| XRD | X-ray diffraction |

**TABLE OF CONTENTS**

M.SC. THESIS EXAMINATION RESULT FORM .....iii

ETHICAL DECLARATION .....iv

ACKNOWLEDGEMENTS .....v

ABSTRACT .....vi

ÖZ .....vii

NOMANCLATURE .....viii

TABLE OF CONTENTS ..... x

LIST OF TABLES .....xii

LIST OF FIGURES .....xiii

**CHAPTER 1 ..... 1**

1.1 Present Positions of Photovoltaic Technology..... 1

1.2 The Properties of SnS Thin Films..... 3

1.3 Sketch of This Thesis..... 8

**CHAPTER 2 ..... 9**

2.1 Absorption of Light..... 9

2.2 Direct and Indirect Band Gap Semiconductors..... 10

2.3 Absorption Coefficient..... 10

2.4 Device Analysis ..... 12

2.4.1 Physics of p-n Junction..... 12

2.4.2 Heterojunction..... 16

2.4.3 Solar Cell Operation..... 17

2.4.4 Solar Cell Properties..... 19

2.5 Photoconductivity of Semiconductors ..... 21

2.6 Electrical Conductivity of Semiconductors ..... 22

**CHAPTER 3 ..... 24**
3.1 Introduction ..... 24
3.2 Deposition of SnS Thin Films ..... 24
3.2.1 Substrate Preparation ..... 24
3.2.2 Grown Process of SnS Thin Films ..... 25
3.2.3 Post-Annealing Treatment ..... 27
3.3 Structural Characterization of SnS Thin Films ..... 28
3.3.1 X-Ray Diffraction (XRD) ..... 28
3.3.2 Atomic Force Microscopy (AFM) ..... 29
3.3.3 Scanning Electron Microscopy (SEM) ..... 31
3.3.4 Energy Dispersive X-ray Spectroscopy (EDS) ..... 32
3.3.5 Thickness Measurement ..... 32
3.4 Electro-Optical Characterization of SnS Thin Films ..... 33
3.4.1 Photoconductivity Measurements ..... 33
3.5 Optical Characterization of SnS Thin Films ..... 33
3.5.1 Transmission Measurements ..... 33
3.5.2 Current-Voltage (I-V) Measurements ..... 34
3.6 Electrical Characterization of SnS Thin Films ..... 35
3.6.1 Electrical Contacts ..... 35
**CHAPTER 4 ..... 36**
4.1 Characterization of SnS Thin Films Deposited on Different Substrates ..... 37
4.1.1 Structural Properties of SnS Thin Films ..... 37
4.1.2 Surface Properties of SnS Thin Films ..... 40
4.1.3 Optical Properties of SnS Thin Films ..... 43
4.1.4 Electrical Properties of SnS Thin Films ..... 46
4.2 Device Characterization ..... 48

**CHAPTER 5- CONCLUSION..... 53**

REFERENCES ..... 52

CURRICULUM VITAE ..... 58

## LIST OF FIGURES

**Figure 1.1** NREL's cell efficiency plot [4] ..... 2

**Figure 1.2** Crystal structure of orthorhombic SnS compound [12] ..... 3

**Figure 2.1** Energy band diagram of semiconductors ..... 9

**Figure 2.2** Direct and indirect band gap of semiconductors [35] ..... 10

**Figure 2.3** The p–n junction in thermal equilibrium for the charge density (Q), the electric field (E), and the voltage (V) plots [6] ..... 14

**Figure 2.4** Energy band diagram of p-type and n-type semiconductors [7-45] ..... 16

**Figure 2.5** The working principle of solar cell [7] ..... 18

**Figure 2.6** Electron hole pairs concentration variation with distance and photocurrent [40] ..... 18

**Figure 2.7** J-V characteristic of solar cell under dark and light conditions [41] ..... 20

**Figure 2.8** (a) ideal p-n junction (b) series and shunt resistances attendant in equivalent solar cell (adopted by reference [43]) ..... 21

**Figure 3.1** Cloverleaf shape mask geometry ..... 24

**Figure 3.2** E-beam evaporation system ..... 26

**Figure 3.3** Overall representation of schematic e-beam evaporation system [46] ..... 26

**Figure 3.4** Annealing furnace ..... 28

**Figure 3.5** XRD system ..... 29

**Figure 3.6** Atomic force microscope ..... 30

**Figure 3.7** SEM measurement device (Hitachi SU5000 model) ..... 31

**Figure 3.8** Dektak 6M Profilometer ..... 32

**Figure 3.9** Perkin-Elmer Lambda 45 Spectrometer ..... 34

**Figure 3.10** I-V measurement system ..... 35

**Figure 3.11** Thermal evaporation system for metal coating ..... 35

**Figure 4.1** XRD pattern of SnS thin films deposited on different substrates ..... 38

**Figure 4.2** SEM micrographs of SnS thin films deposited on a) SLG b) Si c) ITO and d) FTO for 2 μm scale ..... 40

**Figure 4.3** The 2D (left) and 3D (right) 5 μm x 5 μm AFM images for thin film layer deposited on a) SLG, b) Si, c) ITO, d) FTO substrates ..... 42

**Figure 4.4** Transmittance spectra SnS thin films for SLG, ITO and FTO substrates 43

**Figure 4.5** Tauc plots of SnS thin films deposited on SLG, ITO and FTO substrates ..... 45

**Figure 4.6** Temperature dependent photoconductivity of SnS thin films and inset shows temperature range in the dark ..... 46

**Figure 4.7** The photocurrent- illumination intensity at different temperature ..... 48

**Figure 4.8** The schematic diagram of In/p-SnS/n-Si/Ag device structure ..... 49

**Figure 4.9** Temperature dependent current-voltage graph of In/p-SnS/n-Si/Ag structure..... 50

**Figure 4.10** Current-voltage graph of In/p-SnS/n-Si/Ag structure dark and under different illumination intensity at room temperature ..... 52

# LIST OF TABLES

**Table 4.1** The weight and atomic ratios of as-deposited SnS thin films ..... 38

**Table 4.2** XRD analysis results of SnS thin films deposited on different subsrates . 39

**Table 4.3** List of RMS for SnS thin films deposited on different substrates ..... 43

**Table 4.4** Activation energy at different temperature ranges ..... 47

**Table 4.5** Results of temperature dependent I-V analysis of In/p-SnS/n-Si/Ag structure ..... 51

**Table 4.6** Results of I-V analysis of In/p-SnS/n-Si/Ag structure dark and under different illumination intensity ..... 51

**Table 4.7** The solar cell parameters of the p-SnS/n-Si structure ..... 52

# CHAPTER 1

## INTRODUCTION

In this section, the current state of photovoltaic technology is declassified. In addition, the literature review is done by considering the properties of SnS compound. Moreover, information was provided on the motivation and outline of the thesis.

### 1.1 Present Positions of Photovoltaic Technology

Photovoltaic (PV) technology which is used to generate electricity directly from sunlight is one of the most advanced technologies. It is concluded from figure 1.1 that silicone (Si) wafer-based technology is the most widely used PV technology compared to other technologies. However, Si wafer-based technology has a disadvantage due to the high material consumption, limited flexibility and indirect band bap causing some restraints [1], [2]. In this case, thin film PV technologies emerged as an alternative.

Semiconductors such as CdTe, $CuInS_2$ (CIS) and $CuInSe_2$ (CIGS) used in thin film solar cells have high absorption coefficient and direct band gap [3]. As seen in figure 1.1, these materials had a level of efficiency as comparable to Si based solar cells. Although CdTe and CIGS thin film solar cells are popular in the solar market, the scarcity of In, Ga and Te elements in earth crust limits mass production. Consequently, the main limiters for thin film photovoltaic technology are the use of materials that are rare in nature and are toxic.

The devices based on polycrystalline semiconductor thin films have become prominent in technological applications since they are easier to obtain in recent years. Thin film solar cells, optical devices and current industrial applications are the first illustrations where polycrystalline thin films are utilized. Metal chalcogenide nanostructures such as cadmium sulphide (CdS), cadmium selenide (CdSe), zinc sulfide (ZnS), tin sulphide (SnS) etc. have come interesting due to their optical, electronic and superconductor structures in the last few years. In this study, SnS thin

film has been preferred among the materials mentioned above because of its potential technological applications.

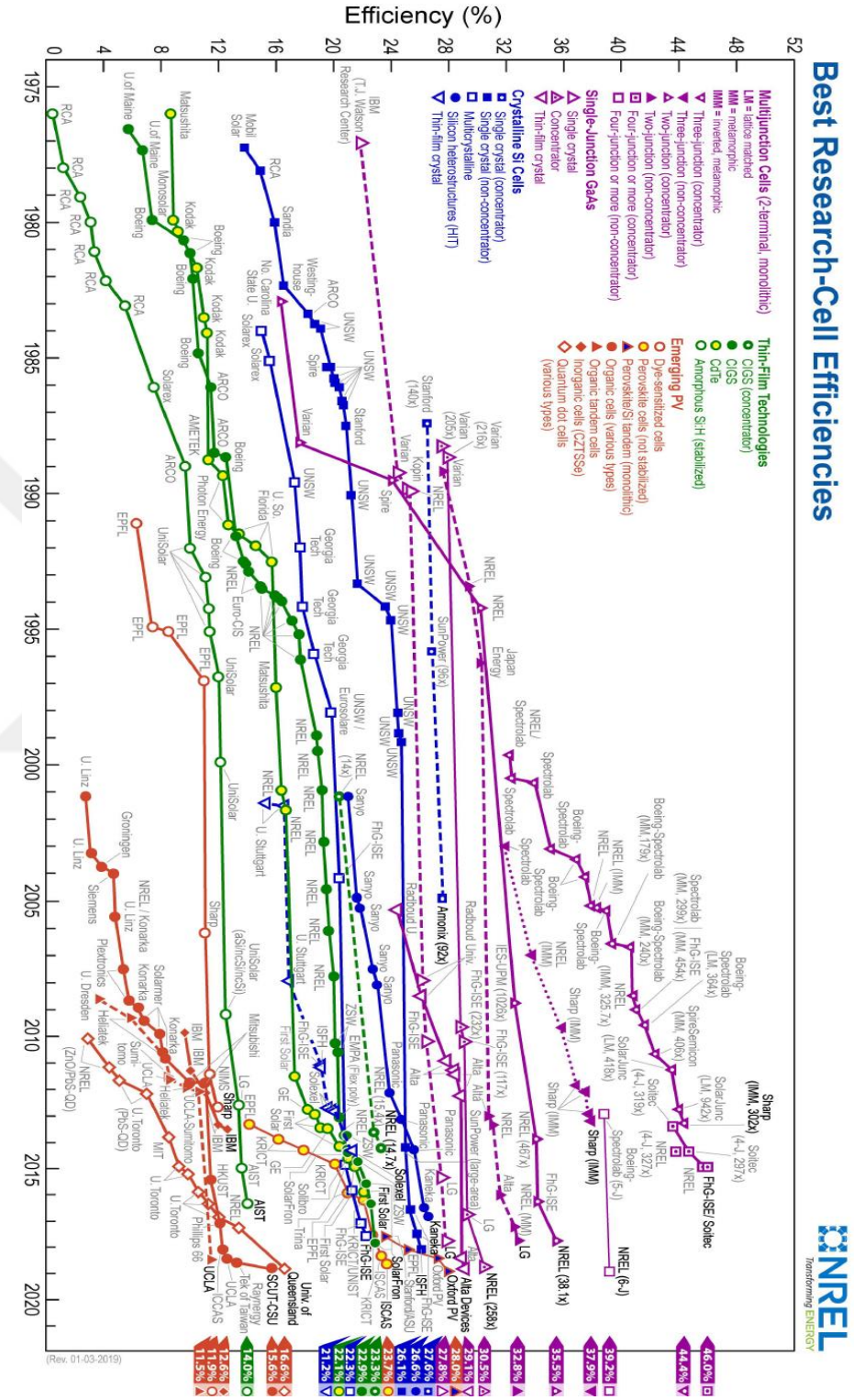



**Figure 1.1** NREL's cell efficiency plot [4]

## 1.2 The Properties of SnS Thin Films

Binary semiconductors are substantial materials by reason of their potential applications in optoelectronic devices, near-infrared (IR) detectors and solar cells [5]. SnS thin films are elements of the IV-VI group which have become remarkable alternative absorber material in recent years [6-7]. Sn and S elements are low cost materials in that they are commonly found in the earth's crust. The compounds such as CdS and CdTe have high efficiency for applications however Cd toxicity is disadvantageous [8]. SnS compound is another feature that allows its non-toxic structure to be preferred. Moreover, compared to compound systems like CIGS, the simple binary systems of SnS structure has better peculiarities for cell production. In the midst of the thin film solar cells, CdTe and CIGS structures have the best efficiency at the literature. The efficiency of these structures has been determined as 21.5% and 23.35%, respectively [9-10-11]. However, the small amount of these materials in nature makes the price quite expensive. This situation prevents commercialization and SnS structure is seen as an alternative material [12].

Crystal structure of SnS demonstrates orthorhombic structure as shown in figure 1.2 [13]. Sn and S atoms are interconnected to each other by Van der Waals bonds and unit cells are stacked as two layers along the c-axis [14].

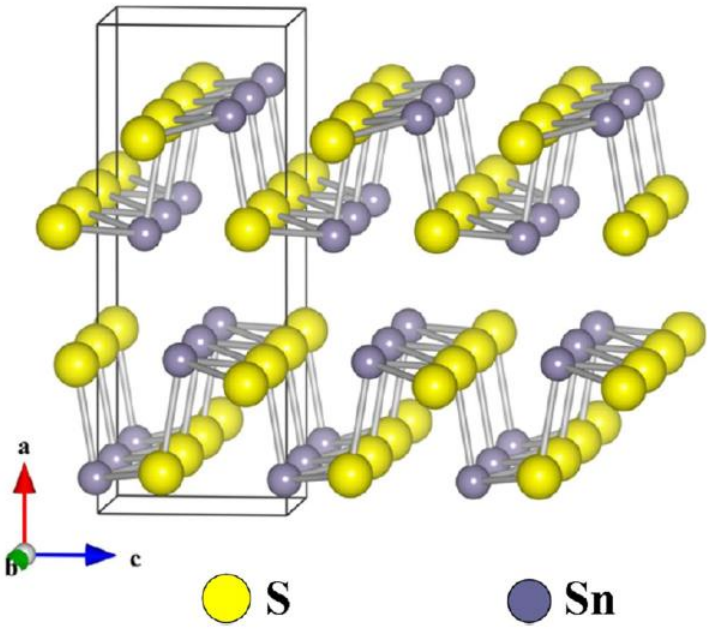



**Figure 1.2** Crystal structure of orthorhombic SnS compound [12]

The band gap of SnS is ranged from 1.1 eV to 2.33 eV depending on the technique and the type of electron transition [12,13]. Both direct and indirect band gap values are optimal energy levels for the absorption of incident light. The SnS compound has a high absorption coefficient ($\alpha > 10^4$ $cm^{-1}$) and low recombination velocity. Furthermore, the ionization energy, work function and electron affinity of SnS is 4.7 eV, 4.2 eV and 3.59 eV, respectively [15]. Compared to classic absorber layers such as CIS and CIGS structure, SnS thin films are more appropriate for ohmic contact due to their low work function and electron affinity. The SnS thin film basic properties are given in figure 1.3.

| Parameters | Values |
|---|---|
| Energy bandgap *Eg* (eV) | $Eg_{direct}$ 1.35 |
| | Reported range (1.00-1.70) |
| | $Eg_{indirect}$ 1.1 |
| | Reported range (1.00-2.33) |
| Absorption coefficient ($cm^{-1}$) | $>10^4$ |
| Refractive index | 1.60-3.52 |
| Conductivity type | *p* Intrinsically |
| | *n* $SnCl_4/CH_3OH$ heat treatment |
| | Isolation ion substitution ($Pb^{2+}$ for $Sn^{2+}$) |
| Intrinsic resistivity (Ω-cm) | 13-20 |
| Rel. dielectric permittivity $\varepsilon_r$ | 13 |
| CB effective density ($cm^{-3}$) | $1.18\times10^{18}$ |
| VB effective density ($cm^{-3}$) | $4.76\times10^{18}$ |
| $e^-$ mobility $\mu_n$ ($cm^2Vs^{-1}$) | 15-25 |
| Hole mobility $\mu_p$ ($cm^2Vs^{-1}$) | 90-100 |
| Acceptor density $N_A$ ($cm^{-3}$) | $10^{17}$ |
| Electron affinity $\chi$ (eV) | 4.20 |
| Work function $\varphi_s$ (eV) | 4.78 |
| Binding energies (eV) | Sn $^3d_{5/2}$ = 485.3, S $^2p_{3/2}$ = 161.4 |
| Crystal structure | Orthorhombic |
| Space group | Pnma, Cmcm |
| United cell volume ($Å^3$) | 192.67 |
| Density ($gcm^{-3}$) | 5.08 |
| Lattice constant (Å) | a = 4.33, b = 11.18, c = 3.98 |
| Bulk modulus (GPa) | ~36.6 |
| Melting point (K) | 1143-1163 |

**Figure 1.3** Main properties of SnS thin film [24]

The SnS thin film presents p-type and n-type conductivity properties subject to the compound's Sn concentration. A small variance in the SnS structure influences the type of conductivity. Stoichiometric SnS compound exhibits p-type conductivity. If the SnS compound is nonstoichiometric, it exhibits n-type conductivity by virtue of S vacancies [16-17]. Due to the p-type conductivity and high absorption coefficient, the SnS main structure is utilized as the absorption layer, while the n-type conductivity and wide band gap are specified as proper features for window layer [17]. The vacancies of S in the SnS thin film is located close to the band gap level and these vacancies have properties that can be recombination center of photogenerated carriers. In contrast, oxygen contaminant can be considered as a trap for the recombination rate at the mid band gap level [18]. Annealing is a process that reduces recombination. With this process, improvements in physical and chemical properties are achieved after the fabrication of the thin films. It causes the growth of particles, resulting in a reduction in grain boundaries, interface, and bulk defects. Likewise, the homogeneity of the thin films is recovered by annealing. There is a noteworthy situation to be considered in the post-annealing process after the fabricated of SnS thin films. At high temperatures upon 300 °C, the Sn phase is resulted to segregate from the SnS compound. Stoichiometric deterioration becomes because of the evaporation of the Sn element at high temperature which directly affects the film properties [19].

The selection of Sn-S based compounds in the formation of photovoltaic p-n and p-i-n structures is convenient due to their optoelectronic properties and 25% power conversion efficiency [20]. Contacts are utilized to analyze the functional status and electrical properties of devices created in optoelectronic applications. The work function ($\phi$) and thermal expansions of the contact metal selected with SnS device must match. The contacts could generally be diversified as metal contact and bilayer contact. Metal contacts are the most commonly used materials such as Ag ($\phi_{Ag}$ = 4.3 eV), Al ($\phi_{Al}$ = 4.25 eV), Pd ($\phi_{Pd}$ = 5.22 eV), Au ($\phi_{Au}$ = 5.10 eV), In ($\phi_{In}$ = 3.83 eV), Sn ($\phi_{Sn}$ = 4.42 eV), Cu ($\phi_{Cu}$ = 4.53 eV), Ni ($\phi_{Ni}$ = 5.01 eV), Mo ($\phi_{Mo}$ = 4.36 eV) [21]. The bilayer contacts such as In/Ag, Cu/Au, Ni/Au materials show Schottky properties. The work function of SnS structure is reported as 4.2 eV in the literature. The SnS structure has changeable contact resistance and it is important to choose a suitable metal as contact. The device should be having low resistance and stable structure. Al, Ag, Au,

In and Zn metals demonstrate perfect ohmic properties in SnS structure [22]. Reddy et al. (2014) investigated the p-SnS/Zn/Ag structure in their study and found that the resistance was decreased [23]. Besides, Patel and Ray et al. (2014) researched more than one metal contact material in their study. They showed that Mo and Ni metals increase the resistance in the SnS device by decreasing the shunt resistance. As a result of this comparison, it is stated that In is the most suitable option [24].

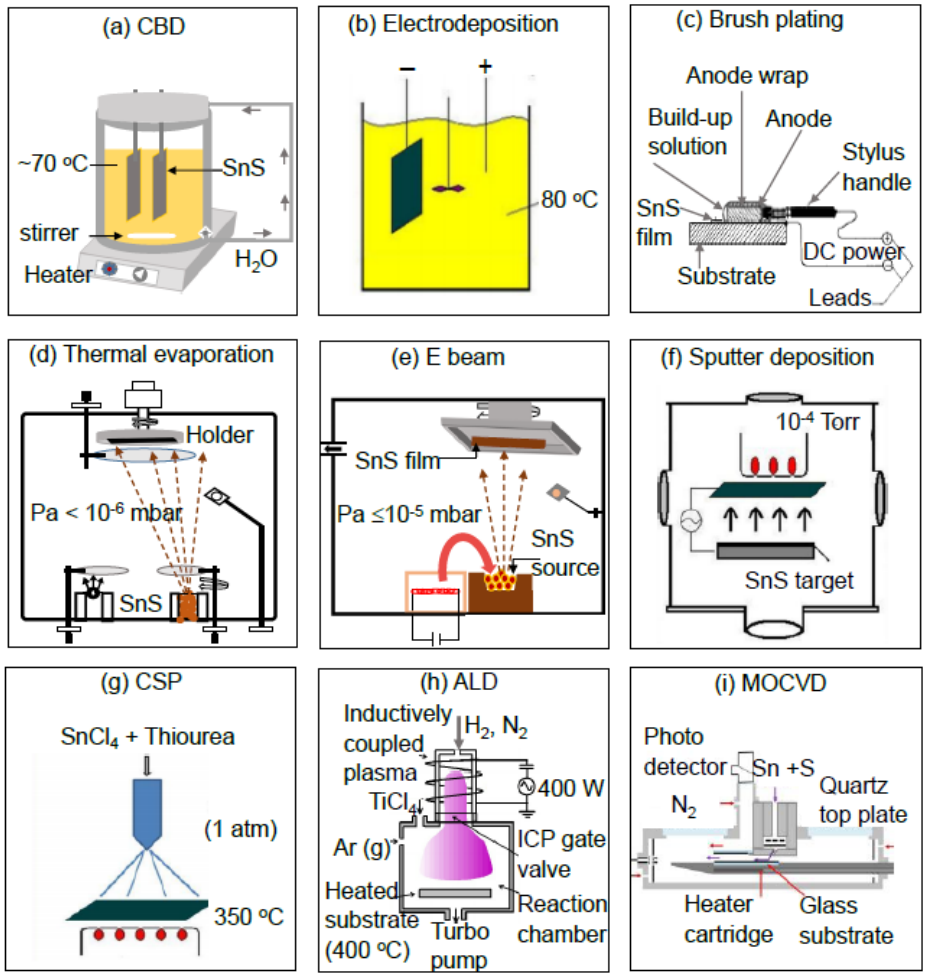



**Figure 1.4** Schematic diagram of SnS thin film deposition method [24]

In recent years, many deposition methods have been used for the fabrication of SnS thin film. The schematic representation of these deposition methods is shown in figure 1.4. Deposition method should be preferred so that grain boundaries and defects are minimized. The reason for this situation is to prevent the formation of potential barriers by reducing recombination. The aim is not to limit charge carriers. Up to now, the highest values in terms of power conversion efficiency have been obtained by physical

methods. ALD and thermal evaporation are methods in which the highest efficiency is acquired [26-27].

As a matter of principle, two factors are crucial for photovoltaic energy conversion. Firstly, the absorption of light is the creation of electron-hole pairs. The second is the separation of the formed electron-hole pairs before recombination. For the second factor, p-n junction is tried to be generated in structures such as SnS. As a result, the most critical step for these two factors is the film's absorbance quality [28]. SnS material was utilized for the first time by Sharon et al. (1988) to observe the photovoltaic potential and the power conversion efficiency (PCE) was determined to be 0.63% [29] Reddy et al. (2006) fabricated SnS based device on glass substrate with chemical spray pyrolysis technique [30]. In the same experimental study, the p-SnS/n-CdS structure was produced using the thermal evaporation method and In contact was coated. In this structure, SnS was utilized as an absorber layer and CdS as a buffer layer. This device showed the best cell parameters at the first. The device's short circuit density ($J_{sc}$) was calculated as 9.6 $mAcm^{-2}$, the open circuit voltage ($V_{oc}$) is 260 mV, the fill factor (FF) is 53% and the efficiency is 1.3% [31]. By fabricating the SnS absorber layer using the thermal evaporation method and utilizing the p-Sns/n-CdS structure, the best efficiency was achieved as 2.53%. By changing the substrate configuration, new record was obtained in the efficiency using alternative materials to CdS. The use of materials with a wider energy band value with SnS is the main reason for these records. Reddy at al. (2015) achieved an efficiency of 2.2% with Mo/SnS/$Zn_{0.76}Mg_{0.24}O$/ZnO: Al/Ag structure [32]. In this study, while sputter was preferred for the production of SnS, $Zn_{0.76}Mg_{0.24}O$ layer was manufactured by chemical spray pyrolysis. The current density vs voltage (J-V) values in the specified structure are as follows: $V_{oc}$ = 575 mV, $J_{sc}$ = 9.96 $mAcm^{-2}$ and FF = 36.4% [32]. The reason for the high $V_{oc}$ value and low Jsc value in this junction has been attributed to the decrease in recombination. After the device design, over 2% power conversion efficiency was recorded by applying heat treatments and arrangement of band alignments. When heat treatment is applied, optimization conditions arise by providing the phase stability of the SnS structure [33]. Sinsermsuksakul et al. (2014) made the SnS synthesis using the ALD method and utilized the SnS/Zn (O, S) structure. In this structure, a 4.4% yield was obtained using a thin layer of $SnO_2$ almost 1 nm thick [25].

This efficiency is a record yield for ALD method. It was obtained by annealing the SnS layers in $H_2S$ to prevent oxidation, increase grain size and reduce recombination losses. The band alignment difficulties of phase absorber films and heterojunctions in the SnS structure are unfavorable for SnS based solar cells. For this reason, only two fabrication methods provided devices with 4% efficiency and higher efficiency. These methods are ALD and thermal evaporation [26].

## 1.3 Sketch of This Thesis

In this thesis, SnS thin films were fabricated by using electron-beam (e-beam) evaporation method. It is aimed to investigate the physical properties of existing mechanisms of SnS structures grown on SLG and silicon substrates. The reasons for the low cost SnS structure to be deposited by e-beam evaporation method are as follows: Firstly, there are high quality SnS thin films fabricated in studies with this method. Secondly, this method is preferred because it is easy to control, low magnification defects and deposition in vacuum environment. The studies in this thesis are divided into five sections:

In the first chapter, information about photovoltaic technology is mentioned. In addition, the current state of thin films is discussed. Afterwards, the properties of SnS compound and related studies are mentioned. In the second chapter, the working mechanism of the solar cell is explained in line with the theoretical information. In the third chapter, thin film deposition methods and measurement techniques used in the thesis are given in detail. In the fourth chapter, it is about the evaluation of the analysis obtained from measurement techniques for SnS thin films. In this section, SnS thin film structure is investigated in detail with the results acquired from the measurements. In the fifth chapter which is the final section, the general evaluation of the thesis is interpreted.

# CHAPTER 2

## THEORETICAL CONSIDERATIONS

This chapter is introduced brief information about semiconductors which forms the theoretical and basic infrastructure of the next sections. Nonetheless, theoretical approaches are made to investigate the results of structural, electrical and optic aspects of the IV-VIA group elements. Lastly, detailed information about diode characteristics of heterojunctions is given and device analysis is revealed.

### 2.1 Absorption of Light

Energy band structure is very significant parameter in semiconductors. The lowest energy level of band is called valance band ($E_V$) and energy level where the electrons can be released is the conduction band ($E_C$). The band gap energy represents the difference between the energy of conduction band and valance band.

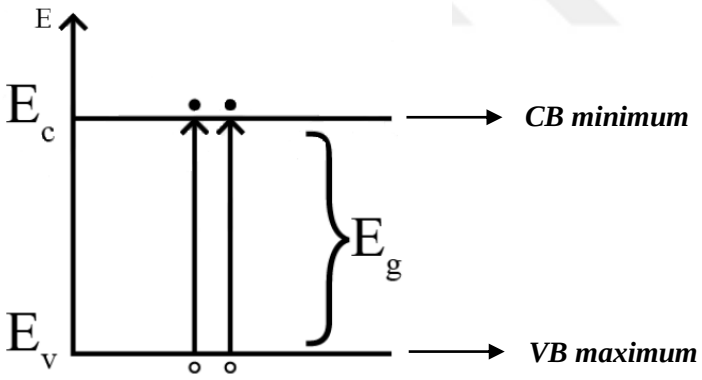



**Figure 2.1** Energy band diagram of semiconductors

The energy band diagram is given in Figure 2.1 and as shown in this figure, the distance between $E_C$ and $E_V$ is called band energy ($E_g$).

The energy band structure of the semiconductors can be examined by means of the optical phenomenon such as absorption, transmission and reflection that take place due to the interaction of the semiconductor with light. Absorption of light could take place in varied transition paths. Besides, the fundamental phenomenon occurs by absorbing

an incident photon with a greater energy than the band energy of the semiconductor [34].

## 2.2 Direct and Indirect Band Gap Semiconductors

The fundamental absorption in semiconductors is inspected in two groups: These are direct and indirect absorption processes which are called optical transitions. Energy and momentum must be conserved during these transitions [35]. In the direct absorption process, the photon is absorbed by electrons in the band gap in the semiconductor. Photon momentum is neglectable compared to electrons. Therefore, electrons starts to move from valance band to conduction band except for any change in photon's momentum. In the indirect absorption process, the momentum of the photon considers and the electrons switch with the photons from the valance band maximum to conduction band minimum. Direct and indirect absorption processes are shown schematically in figure 2.2.

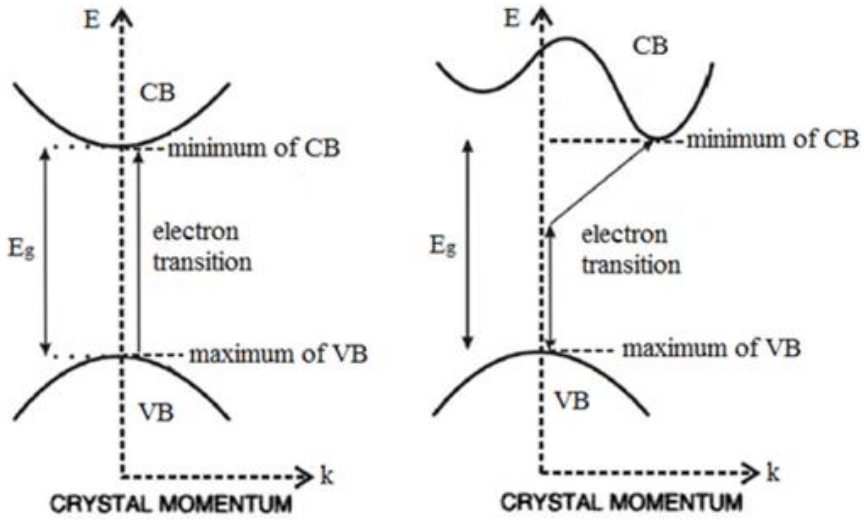



**Figure 2.2** Direct and indirect band gap of semiconductors [35]

## 2.3 Absorption Coefficient

The band gap of semiconductors is determined through optical analysis. In optical characterization, the transmission (T) and reflection (R) of a material are usually

measured. The absorption coefficient (α) of a sample could be found by use of the following equation 2.1:

$$T = \frac{(1-R)^2\, e^{-\alpha d}}{1 + R^2\, e^{-2\alpha d} - 2Re^{-\alpha d}\cos\varphi} \quad \textbf{(2.1)}$$

where d is thickness of sample, the expression in the cosine is used to determine the detection and spectral frequency property which its explanation is given the below,

$$\varphi = \frac{4\pi n d}{\lambda} \quad \textbf{(2.2)}$$

where n is refractive index, λ is incident wavelength of radiation and R is reflectance of sample as,

$$R = \frac{(n_0 - n_s)^2 + k^2}{(n_0 + n_s)^2 + k^2} \quad \textbf{(2.3)}$$

where $n_0$ is the refractive index of the substrate, $n_s$ is the refractive index of sample and k is the extinction coefficient. α and k are interrelated. α can be expressed with equation 2.4,

$$\alpha = \frac{4\pi k}{\lambda} \quad \textbf{(2.4)}$$

If the energy of incident photon is greater than $E_g$, the semiconductor material is assumed to be transparent and hence $\alpha \approx 0$. In this condition, equation 2.5,

$$T = \frac{(1-R)^2}{1 + R^2 - 2R\cos\varphi} \quad \textbf{(2.5)}$$

The spectral frequency can be neglected due to the resolution of the measurement being performed. Therefore, when the semiconductor transmission values can be written again,

$$T = \frac{(1-R)^2}{1-R^2} = \frac{1-R}{1+R} \quad \textbf{(2.6)}$$

In addition to this, impurities in the material also play a role in the absorption of photons. In the form below, the relationship between the density of impurities and α is given in equation 2.7,

$$T = \frac{(1-R)^2 e^{-\alpha d}}{1 + R^2 e^{-2\alpha d}} \tag{2.7}$$

Hence, α can be written in the form below,

$$a = -\frac{1}{d}\left(\frac{\sqrt{(1-R)^4 + 4T^2R^2} - (1-R)^2}{2TR^2}\right) \tag{2.8}$$

On the basis of fundamental absorption in semiconductor, the reflection and interference effect are neglected when switching from band to band. For this reason, the absorption coefficient in simplest form,

$$\alpha = \frac{1}{d}\ln(T) \tag{2.9}$$

Absorption and band gap concern based on semiconductor electron motion that occurred due to doable transition in the previous section,

$$\alpha \sim (h\nu - E_g)^{\gamma} \tag{2.10}$$

Here, hν is the energy of incident photon. γ is constant value which can change according to the transition characteristic. The γ value takes ½ in direct transitions and the transitions take place vertically. This value is 2 in indirect transitions. According to Tauc plots, $(\alpha h\nu)^2$ vs hν is plotted for direct band gap semiconductors and also $(\alpha h\nu)^{1/2}$ vs hν is plotted for indirect band gap semiconductors. Then, the points where the graphs intersect the energy axis give the band gap value of the materials [36].

## 2.4 Device Analysis

### 2.4.1 Physics of p-n Junction

Semiconductors are categorized as n-type and p-type materials. It is known that the electron concentration of n-type semiconductors is greater than hole concentration. However, this situation is the opposite in p-type semiconductors. In other words, n-

type semiconductors have electrons in majority whereas p-type semiconductors have electrons in minority. In n-type semiconductors, the Fermi energy level is closer to the conduction band than valance band. Since this is the opposite of p-type semiconductors, the Fermi energy level is closer than valance band than conduction band [37]. If n-type and p-type semiconductors are in contact, p-n junction is formed between them. While creating the same semiconductor homo-junctions with different doping types, particular semiconductors create hetero-junctions with different doping types. By the reason of difference of carrier concentration on both sides, the formation of junction as result diffuses electrons from the n-type region to the p-type region and also the holes from the p-type region to the n-type region. Electrons diffusing from the n-type region combine with the holes. In a similar way, the holes diffusing from the p-type region combine with the electrons.

Current is formed in the junction area due to diffusion. The space charge region comprises by the opposite charge called donor and acceptor at the junction area is shown in figure 2.3. A negatively charged area in the n-type region and a positively charged area in the p-type region are formed. Therefore, an internal electric filed occurs in the junction region. This internal electric field take places in the opposite direction of diffusion and thus occurs in an equilibrium state. Eventually, there is no net current in p-n junction region. So the diffusion current of electrons at the junction in equilibrium is balanced with the drift current of electrons. Likewise, the diffusion current of holes is balanced with the drift current. This equilibrium is given as follow equation 2.11 and 2.12 [38],

$$J_p(drift) + J_p(diffusion) = 0 \quad \textbf{(2.11)}$$

$$J_n(drift) + J_n(diffusion) = 0 \quad \textbf{(2.12)}$$

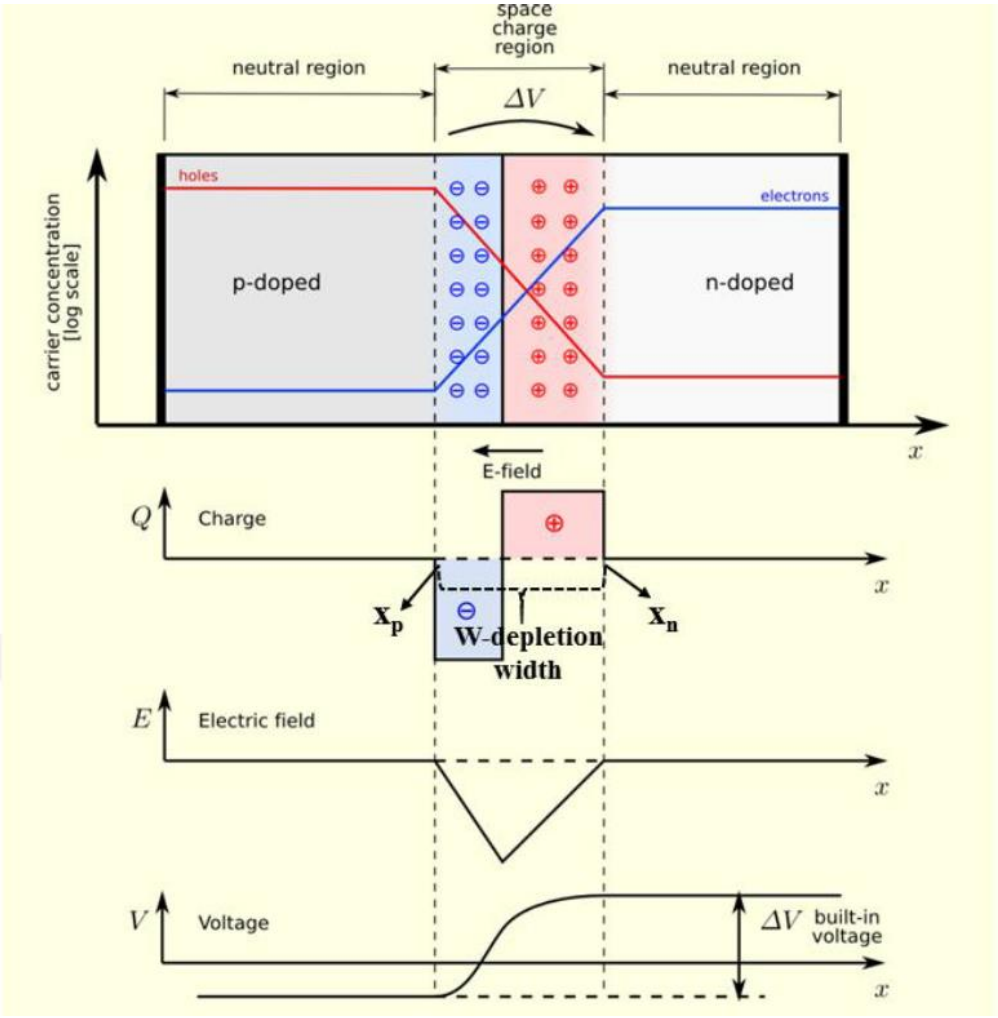



**Figure 2.3** The p–n junction in thermal equilibrium for the charge density (Q), the electric field (E), and the voltage (V) plots [6]

Figure 2.3 seems the charge density (Q), electric field (E), and voltage (V) graphs of p-n junction. A potential difference occurs when equilibrium is reached in p-n junction region and this potential difference is called "built-in" potential ($V_b$). The depletion region width (W) is calculated from the analysis of the Poisson's equation using depletion region approach [38], $X_p$ and $X_n$ are included in this approach. $X_p$ represents the transition width on the p-side and $X_n$ on the n-side. The $X_p$ and $X_n$ values are determined for the two semiconductor layers and the Poisson's equation is concluded according to the coordinate of the interface.

$$W = \left[\frac{2\varepsilon(N_a + N_d)V_0}{qN_aN_d}\right]^{1/2} \quad \textbf{(2.13)}$$

$$X_p = \left[\frac{2N_a\varepsilon_r\varepsilon_0V_b}{qN_d(N_a + N_d)}\right]^{1/2} \quad \textbf{(2.14)}$$

$$X_n = \left[\frac{2N_d\varepsilon_r\varepsilon_0V_b}{qN_a(N_a + N_d)}\right]^{1/2} \quad \textbf{(2.15)}$$

$\varepsilon_r$ and $\varepsilon_o$ given in the equation 2.14 and 2.15 are dielectric constant.

When the formulas given in the explanation are brought into the simplest form,

$$N_aX_p = N_dX_n \quad \textbf{(2.16)}$$

With this equation 2.16, it is concluded that high doped material has narrow depletion region and low doped materials have large depletion region.

The built-in voltage ($V_b$) is expounded as,

$$V_b = \frac{k_BT}{q}\ln\left(\frac{N_aN_d}{{n_i}^2}\right) \quad \textbf{(2.17)}$$

where $k_B$ is Boltzmann's constant, T is temperature, q is charge of carrier and $n_i$ intrinsic carrier concentration of semiconductors.

The electron and hole density consist of the sum of the drift and diffusion current in the junction region. The neutral part of the p-type region and the current density in the depletion region of electron ($J_n$) can be express by ideal diode equation 2.18 as follows:

$$J_n = -\frac{qD_nn_{p0}}{L_n}\left[exp\left(\frac{qV}{k_BT}\right) - 1\right] \quad \textbf{(2.18)}$$

$D_n$, $n_{n0}$ and $L_n$ are represented electron diffusion coefficient, electron concentration of in the equilibrium at the p-side, electron diffusion length, respectively. In a similar manner, the hole current density ($J_p$) is the consequence of the equation 2.18 minus sign and represents the current in the opposite direction:

$$J_p = -\frac{qD_pn_{n0}}{L_p}\left[exp\left(\frac{qV}{k_BT}\right) - 1\right] \quad \textbf{(2.19)}$$

$D_p$, $n_{p0}$ and $L_p$ are represented hole diffusion coefficient, hole concentration of in the equilibrium at the n-side, hole diffusion length, respectively. Total current density ($J_{total}$) at the junction depending on the given equations 2.20 and 2.21,

$$J_{total} = J_n + J_p = q\left(\frac{D_n n_{p0}}{L_n} + \frac{D_p n_{n0}}{L_p}\right)\left[exp\left(\frac{qV}{k_B T}\right) - 1\right] \quad \textbf{(2.20)}$$

$$J_{total} = J_0\left[exp\left(\frac{qV}{k_B T}\right) - 1\right] \quad \textbf{(2.21)}$$

where $J_0$ is the reverse saturation current density.

### 2.4.2 Heterojunction

The heterojunction band model is created using abrupt-band model. In composition of the heterojunction model, the $X$, $E_g$ and $\Phi$ of the two-constituent semiconductor material are considered.

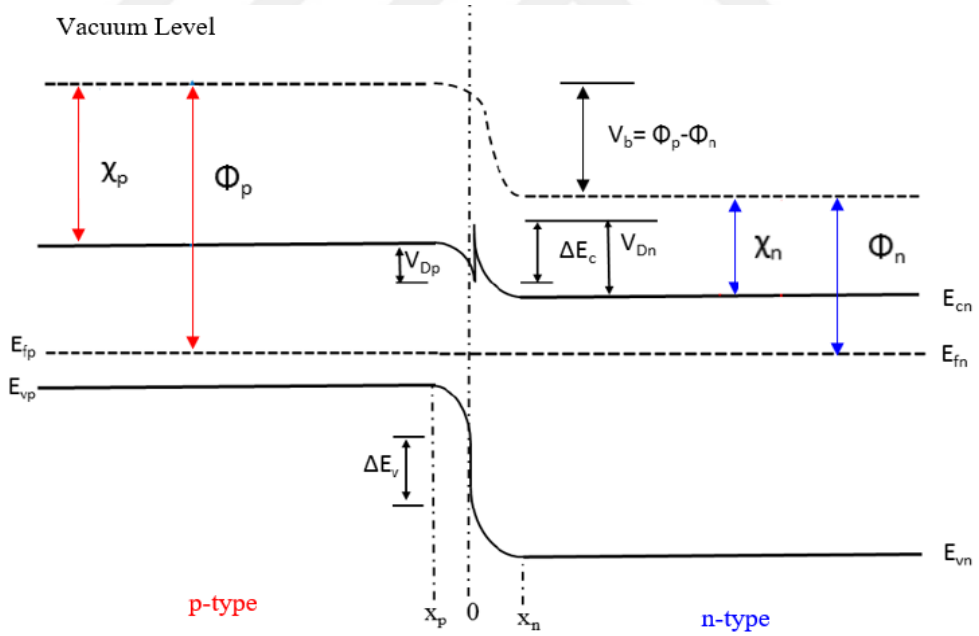



**Figure 2.4** Energy band diagram of p-type and n-type semiconductors [7-45]

Figure 2.4 seems the energy band diagram of two semiconductors with equilibrium and vacuum levels. This band diagram shows that n-type semiconductor's $E_g$ is greater than the p-type's band gap ($E_{gn}$>$E_g$). When $E_g$ of p-type semiconductor is greater than n-type semiconductor ($E_{gp}$>$E_g$), it shows the n-type characteristic. In addition, its

properties such as work function ($\Phi_p$,$\Phi_{n)}$, dielectric constants ($\varepsilon_p$, $\varepsilon_n$) and electron affinities ($\chi_p$, $\chi_n$) are considered to be particular. The difference of $\Phi$ gives the $V_b$ and this potential is shown in figure 2.4 as $V_b = \Phi_p - \Phi_n$. $V_{Dp}$ and $V_{Dn}$ represent relative band bending and their sum is equivalent to the built-in potential, respectively.

The difference in conduction band of semiconductors gives the difference in $\chi$ and in response to this conduction band offset ($\Delta E_c$) given with equation 2.22,

$$\Delta E_c = \chi_p - \chi_n \quad \textbf{(2.22)}$$

In the valance band offset $\Delta E_v$ is found as,

$$\Delta E_v = E_{gn} - E_{gp} - \Delta E_c \quad \textbf{(2.23)}$$

Band gap of semiconductors is obtained by sum of both discontinuities and given as,

$$\Delta E_g = \Delta E_c + \Delta E_v = E_{gn} - E_{gp}$$

### 2.4.3 Solar Cell Operation

The working principle of a solar cell is given in figure 2.5 as the schematic diagram. When the incident photon energy is greater than band gap energy ($E_g \leq E_{photon}$), the photon is absorbed by the semiconductor and electron hole pairs are generated. With p-type and n-type semiconductors forming contact zone, a built-in electric field located at the junction area. The internal electric field separates the electron hole pairs. With the effect of built-in electric field, electrons are drifted to the semi-neutral n-type region and this region becomes negatively charged. Likewise, the holes are drifted to the semi-neutral p-type region with the effect of the built-in electric field and make this region positively charged. As a result, a $V_{oc}$ generates in the solar cell. By connecting an external charge, the excess electrons in the n-type semi-neutral region complete the circuit and reach the p-type semi-neutral region. The excess holes which found in this region are recombine into electron hole pairs.

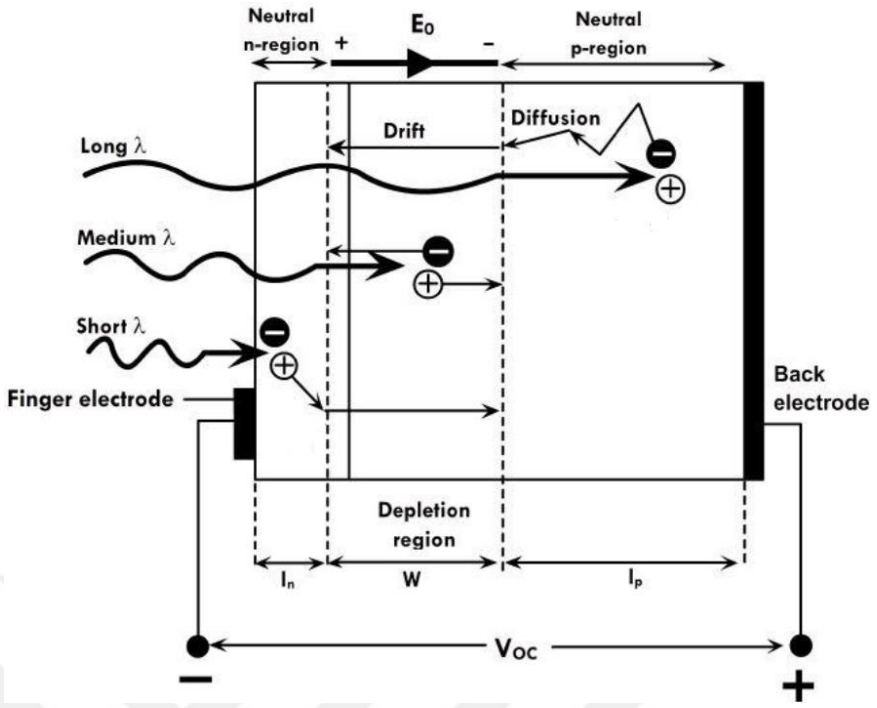



**Figure 2.5** The working principle of solar cell [7]

In case of short circuit of the solar cell, the sole current in the circuit is caused by flow of electron hole pairs. This current is called photocurrent ($I_{ph}$) and is shown in figure 2.6. Another name for this current is short circuit current which is presented in opposite direction $I_{sc}$. These currents should be reversed according to the definitions and given as $I_{ph}= -I_{sc.}$ In the presence of an external R load in the solar cell circuit, a voltage generates.

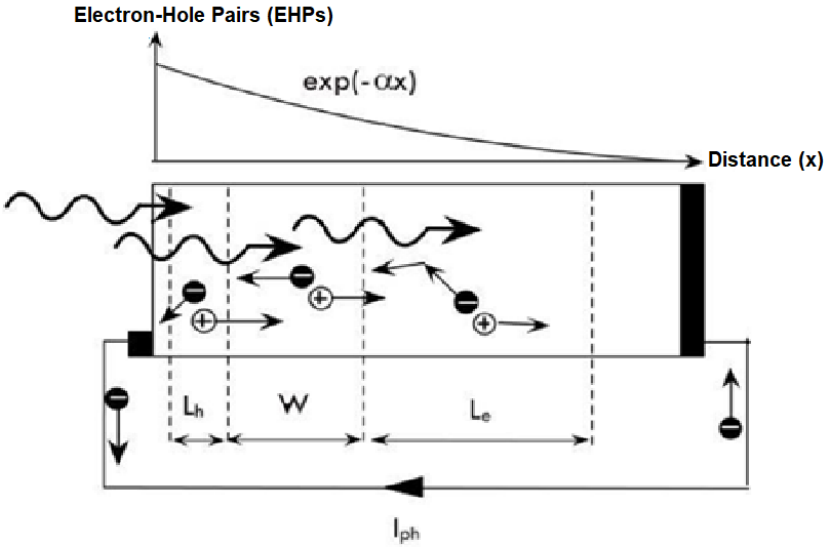



**Figure 2.6** Electron hole pairs concentration variation with distance and photocurrent [40]

An ideal solar cell can be considered as diode sensitive to photovoltaic effect. The current-voltage (I-V) properties of ideal diode can be explained by Shockley solar cell equation.

$$I = -I_{ph} + I_0 \left[ exp\left(\frac{qV}{nkT}\right) - 1 \right] \quad \textbf{(2.24)}$$

where $I_0$ is diode saturation current, q is charge of electron, V is external voltage, n is ideality factor, T is absolute temperature.

In case of an open circuit, the total current becomes zero and is expressed as follows,

$$I_{ph} = I_0 \left[ exp\left(\frac{qV}{nkT}\right) - 1 \right] \quad \textbf{(2.25)}$$

When the following assuming equation 2.26 is applied to $V_{oc}$, equation 2.27 is obtained.

$$V_{oc} \gg \frac{nkT}{q} \quad \textbf{(2.26)}$$

$$V_{oc} \approx \frac{nkT}{q} \ln\left(\frac{I_{ph}}{I_0}\right) \quad \textbf{(2.27)}$$

It can be concluded from equation 2.27 that $I_0$ and $V_{oc}$ change inversely.

### 2.4.4 Solar Cell Properties

The current per unit area is called $J_{sc}$ and this current density is shown in figure 2.7. The photovoltaic properties of solar cell are characterized by the curve given in figure 2.7. $J_{sc}$ is a short circuit current density and is caused by the illumination of solar cell. The $J_{sc}$ value is located on the curve at the point corresponding to the value V=0.

The $V_{oc}$ is another substantial parameter and represents the potential difference between the finger and back contact of the solar cell. Indeed, the illuminated solar cell is the output voltage even as there is no current in the cell.

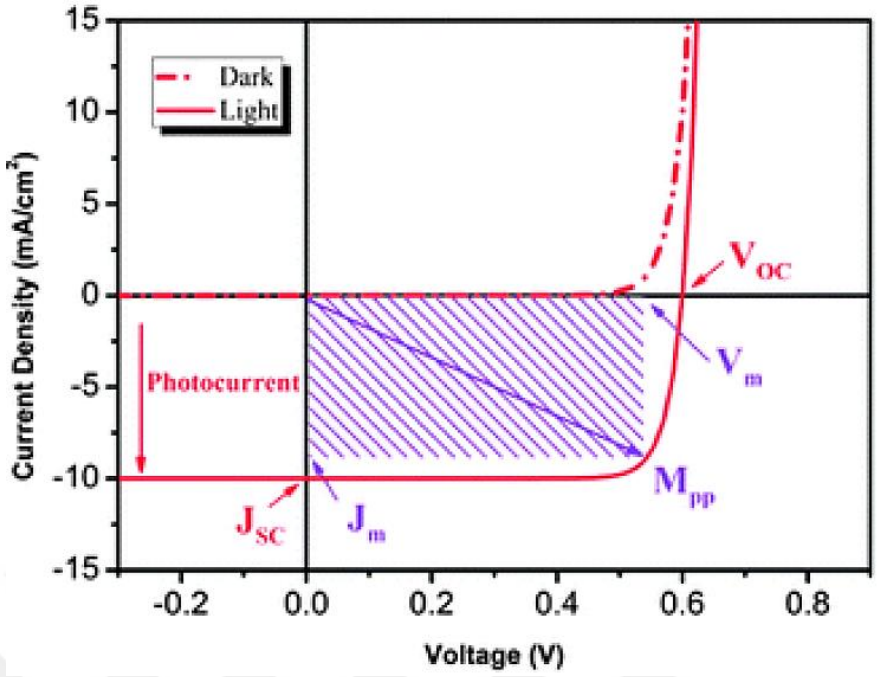



**Figure 2.7** J-V characteristic of solar cell under dark and light conditions [41]

The maximum power point ($M_{pp}$) is calculated from maximum photocurrent ($J_m$) and maximum open circuit voltage ($V_m$) points. The standard of the quality of a solar cell is determined by FF. The fill factor of a solar cell is given as [42],

$$FF = \frac{I_{max}V_{max}}{I_{sc}V_{oc}} = \frac{P_{max}}{I_{sc}V_{oc}} \quad \textbf{(2.28)}$$

Power conversion efficiency (η) is the ratio of the maximum output energy of a solar cell ($P_{max}$) to the input energy obtained by solar radiation and found as equation 2.29,

$$\eta = \frac{P_{max}}{P_{in}} = \frac{I_{max}V_{max}}{P_{in}} = \frac{I_{sc}V_{oc}FF}{P_{in}} \quad \textbf{(2.29)}$$

Ideal solar cells may in some cases vary in p-n junction properties. $R_s$ and $R_{sh}$ can be ignored in ideal solar cells. The equivalent circuit of an ideal solar cell in (a) part of figure 2.8 and the non-ideal solar cell in (b) part is illustrated. In figure 2.8 (a) part, the external load resistance ($R_L$) is included in the system and the diode current ($I_d$) is shown. The $R_s$ is revealed with the total current and resistance in the device. $R_s$ decreases the solar cell's FF and affects the device quality. Besides, this resistance can limit the $I_{sc}$ but has no effect on the $V_{oc}$. So as to an ideal solar cell, the $R_s$ must have to be low and high $R_{sh}$ is opted for the equivalent circuit. Because $R_s$ and $R_{sh}$ are the

leakage current measurement of solar cell. High $R_{sh}$ prevents leakage current while low shunt reduces $V_{oc}$.

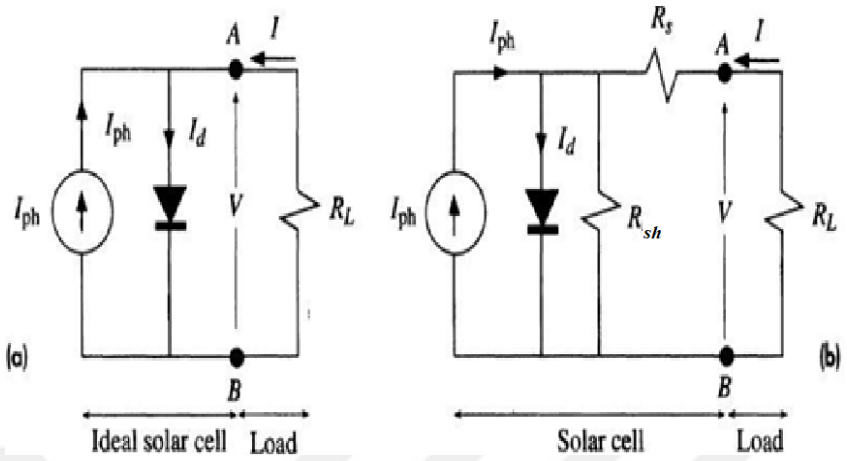



**Figure 2.8** (a) ideal p-n junction (b) series and shunt resistances attendant in equivalent solar cell (adopted by reference [43])

## 2.5 Photoconductivity of Semiconductors

The statement of photoconductivity is a variation of the electron hole pairs with the change in the number of free carriers of a semiconductor material under illumination. When measuring photoconductivity, external voltage is applied to the contact of the material. The current formed by the application of this voltage is measured in dark and illuminated conditions. If the incident photon energy is greater than $E_g$, free carriers occur and this raises the conductivity of the semiconductor. Recombination of carriers is a condition that limits the conductivity of semiconductor material [44]. As the electron hole pairs generation and recombination occurrences are balanced with each other, the state of photoconductivity becomes stable. This equilibrium state can be explained by following equation 2.30 [45],

$$-\frac{dn}{dt} = Anp = An_0p \qquad \textbf{(2.30)}$$

In this equation, A is a constant value and $n_0$ represents the electron density. The excess carrier density is given equation 2.31 as,

$$n(t) = n(0)exp\left(-\frac{t}{\tau}\right) \qquad \textbf{(2.31)}$$

where τ is recombination lifetime and formula are as follows,

$$\tau = (An_0)^{-1} \quad \textbf{(2.32)}$$

In steady state, photoconductivity is calculated with the formula 2.33 below,

$$\sigma_{ph} = q\emptyset_p \alpha \mu \tau \quad \textbf{(2.33)}$$

where $\emptyset_p$ is the incident photon flux. $\emptyset_p\alpha$ is approximately equal to generation rate of free carriers (G) and this case is given as $G \approx \emptyset_p\alpha$.

## 2.6 Electrical Conductivity of Semiconductors

The electrical conductivity ($\sigma$) of a material is a measure of how well electronic carriers transport. Materials are classified as conductors and insulators according to their electrical conductivity. In insulators, resistances are applied in response to the flow of electric current. In conductors, electric current can flow freely. Besides, semiconductor materials emerge by thermal stimulation of insulating materials. The valance band of semiconductors is filled with electrons at 0 K temperature and there are no charge carriers in the conduction band. Semiconductors at a temperature higher than 0 K have free charge carriers in the conduction band. The conductivity value of semiconductors is very low compared to insulators and very high compared to conductors. Electrical conductivity can be measured using the van der Pauw method or 4-point probe. Resistivity ($\rho$) can be found using these measurement systems. Since the current in the semiconductor is provided by electrons and holes, the conductivity ($\sigma$) statement is as follows:

$$\sigma = ne\mu_e + pe\mu_p \quad \textbf{(2.34)}$$

In equation 2.34, μ is mobility, n is free electron concentration and p is free hole concentration. Mobility is the motion of an electron in a metal or semiconductor under the electric field. The density of electrons that are not bound to any ion or atom in the conduction band is called the free electron concentration. Likewise, the density of free holes in the valance band is called free hole concentration. In intrinsic semiconductors, these concentrations are equal in the conduction band and valence band.

$$\mu = \frac{\upsilon_d}{E} \quad \textbf{(2.35)}$$

where $\upsilon_d$ is defined the drift velocity and E is applied electric field.

$$n = p = constant\ x\ T^{3/2}\ exp\left[\left(-E_g\right)/2k_BT\right] \quad \textbf{(2.36)}$$

Conductivity can be written from equation 2.37 and 2.38 as follows.

$$\sigma = constant\ xe\ (\mu_e + \mu_h)T^{3/2}\ exp\left[\left(-E_g\right)/2k_BT\right] \quad \textbf{(2.37)}$$

Then energy band gap is obtained from slope of $T^{-1}$ versus In ($\sigma_0$) which is pre-exponential valence:

$$\sigma = \sigma_0\ exp\left[\left(-E_g\right)/2k_BT\right] \quad \textbf{(2.38)}$$

# CHAPTER 3

# EXPERIMENTAL TECHNIQUES

## 3.1 Introduction

In this chapter, the methods and equipments used to produce and characterize SnS thin films is identified in detail. Firstly, preparing process of substrates and thin film production methods is explained. In the other respects, electron beam evaporation technique which is the deposition method of SnS thin films is summarized. In the following part, the electrical, optical and structural characterization processes of fabricated thin films are discussed in detail.

## 3.2 Deposition of SnS Thin Films

### 3.2.1 Substrate Preparation

SnS thin films were grown SLG, ITO, FTO and Si substrates. The substrate size varies according to the substrate holder of the devices to be characterized. Samples of 1cmx1cm size were used for characterization in scanning electron microscopy (SEM), energy dispersive spectroscopy (EDS), atomic force microscopy (AFM) and 2cmx2cm samples were used for characterization in X-ray diffraction (XRD) and ultraviolet-visible (UV-Vis). Van der Pauw method was used as the main measurement technique in electrical characterization and it is suitable geometry was produced in order to obtain a successful measurement. Masking has been done to create this cloverleaf shape and this mask is shown in Fig. 3.1 below:



**Figure 3.1** Cloverleaf shape mask geometry

Van der Pauw is a common method that enables I-V experiments using four points selected on the sample. It has become a standard method resulting from the reduction of measurement errors due to distance differences.

The cleaning procedure to be applied the substrates is critical. In that, pin-holes and contaminations that bring about on thin films surface will affect the film quality negatively. Glass and Si substrates were kept separately in acetone. After rinsing, it was placed in an ultrasonic bath with hot distilled water. After this stage, cleaning was continued with a mixture of hot water and detergent in order to remove impurity from the substrate surfaces. At the end of each stage, rinsing was repeated with hot distilled water and acetone. Ultrasonic bath treatment was performed with isopropanol to remove residual waste and detergent residues. Samples were placed in 30% $H_2O_2$ solution and cleaned with ultrasonic bath to detract from the surface for organic impurities. After this procedure, it was rinsed with hot distilled water. At the end of the cleaning procedure, samples dried with nitrogen gas and made ready for use.

### 3.2.2 Grown Process of SnS Thin Films

At the present time, thin film production methods have need for a physical vapor deposition (PVD) environment. PVD is the oldest and the most common method of production in the vacuum environment. This method has been preferred because it is easy to apply and controllable. The general working principle of the PVD method is as follows: Firstly, the source material is evaporated and then the fabrication is made on the substrate with help of the condensation process. Although the basic working principle is the same, PVD technique is divided into classes according to the evaporation method of the source material and there are several types of PVD. The first is thermal evaporation and the source material evaporated by heating with a heating coil in the area on which it is placed. The second is the e-beam evaporation method and the source material are evaporated with electron flux. The third is sputtering method and the source material is sputtered with high energy gas.

The e-beam thermal evaporation system utilized for the production of SnS thin films is shown in figure 3.2. In this fabrication method, the electron beam is accelerated by

performing high voltage to the filament. The source material is evaporated with the electron beam having this high energy and it is coated on the substrate in a layer.



**Figure 3.2** E-beam evaporation system

The schematic representation of the e-beam evaporation system preferred in this thesis work shown in figure. 3.3. The system consists of equipments which are given in the figure description.

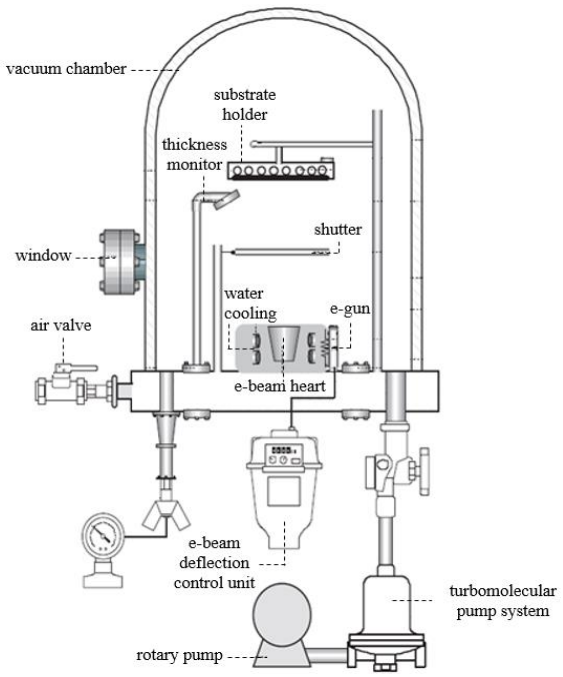



**Figure 3.3** Overall representation of schematic e-beam evaporation system [46]

The grown process started with the placement of glass, ITO, FTO and Si substrates in the holder at a distance of 30 cm from the deposition source in the vacuum chamber. Source pellet of SnS was embeded in graphite crucible and a boat, respectively. The shutter is kept closed before coating process. The deposition rate and thickness of the films were monitored during the process using Inficon XTM/2 deposition monitor which was added to the system afterwards. The coating of SnS thin films was implemented under a pressure of approximately $1.6x10^{-6}$ Torr. Firstly, Varian 3117 rough pumping vacuum system was used to reach high pressure like $10^{-2}$ Torr. Following this process, the Leybold turbomolecular pump system was operated to provide the pressure condition required for fabrication. The basic principle of e-beam production is to apply current to the source material with electron emission. With this electron emission, the source material was evaporated and shutter was opened when the source material starts to evaporate. The deposition rate was pursued on the monitor and this value is kept constant at approximately 4-6 Å/s. After the films reach the requested thickness, the shutter and power supply of the e-beam system was turned off, respectively. After these processes, first of all turbo and then mechanical pump was shut down. Finally, sufficient time was waited to prevent oxidation and the vacuum was broken.

### 3.2.3 Post-Annealing Treatment

After annealing process the deposited thin films are widely used as it provides a reduction in film stress and structural improvement [47]. In this study, post annealing process impresses as grown deposition proceedings on the SnS thin films were inspected.

In such a treatment, the as grown thin films were positioned in a horizontal and isolated Lindberg type furnace as shown in figure 3.4. As grown samples were positioned in the center of furnace and the temperature was gradually increased. Nitrogen ($N_2$) gas flow is provided in the furnace to prevent contaminations that may occur during the annealing process and turned off when all processes are finished. The annealing temperature value was preserved for a certain time period and the system was allowed to cool slowly to room temperature.



**Figure 3.4** Annealing furnace

In a part of this thesis, this process was used after the electrical contacts were coated using thermal evaporation method. Post-annealing makes the coated contacts with the substrate interface more effective. It is also preferred to prevent the contacts from detaching from the surface in the next step.

## 3.3 Structural Characterization of SnS Thin Films

### 3.3.1 X-Ray Diffraction (XRD)

X-ray diffraction (XRD) one of the most common and powerful techniques used in science of materials to specify the crystal structure, distance between atoms and lattice orientations of material. In this analysis method, X-rays are sent to the material and diffraction indices on the material surface are analyzed. Fundamentally, the diffraction profile pattern formed after X-rays are sent to the surface provides evidence for the atomic structure. By comparing the profiles of materials, information about the atomic structure is provided. X-rays have wavelengths from 0.1 through 100 Å. The most commonly used wavelength range in this method is about 0.5 to 2.5 distance between atoms in solid materials.

XRD analysis of fabricated SnS thin films were analyzed using the Rigaku Miniflex XRD system shown in figure 3.5. XRD scans were taken 2θ ranging from 10 to 90° with a 2°/minute using Cu-Kα radiations (λ=1.54 Å). The diffraction pattern data was

analyzed by Rigaku's software program. This program contains reference patterns and analysis is performed by matching ICDD card database. Apart from that, the experimental data can also be investigated using the literature.



**Figure 3.5** XRD system

The XRD working principle is based on Bragg's Law [48]:

$$n\lambda = 2d \sin \theta \quad \textbf{(3.1)}$$

As the above formula is rearranged by accepting n for a minimum (n=1),

$$n\lambda\ 2d = \sin \theta \leq 1 \quad \textbf{(3.2)}$$

$$\lambda \leq 2d \quad \textbf{(3.3)}$$

where n is reflection, $\lambda$ is the wavelength of X-rays, $\theta$ is angle of incident beams and d is interplanar spacing. In this work, peak investigation and matching was performed by analyzing at the peak intensities and positions at $2\theta$ values.

### 3.3.2 Atomic Force Microscopy (AFM)

Atomic force microscopy (AFM) is a surface scanning method utilised to obtain information about surface topographic properties of samples. An AFM device has a sharp tip console, laser, scanner and photodetector. Using this equipment, the forces formed between the sample surface and cantilever tip are measured in nanoscale. These forces are magnetic, electrostatic and Van der Waals bonded forces [4]. The

surface scan movement is relying on the interactive relation between the sample surface and the tip. The movement is followed by projecting the laser beam onto the photodetector. AFM images are obtained from the photodetector output voltage as a final process.



**Figure 3.6** Atomic force microscope

In this work, SnS thin films measurements were done by using AFM of METU Central Laboratory. AFM has three types of operation modes and tapping mode was used in this study. In this mode, the tip slides across the surface in three dimensions and is the most effective mode. At the same time, the drift motion of the tip on the sample can damage for both the sample and the tip. In tapping mode, the forces generated by dragging are measured together with instant contact among the tip and the surface. Image quality is high due to multiple force measurements. In non-contact mode, Van der Waals forces are measured between the tip and the surface. As these forces are less attractive and the image quality is low. AFM measurements were performed using the Veeco MultiMode V AFM shown in figure 3.6. AFM images of the surfaces with 5μm X 5μm area were taken as 2D and 3D.

### 3.3.3 Scanning Electron Microscopy (SEM)

SEM is a widely used method in micro analysis to investigate the topographic and morphological properties of materials. Electron beam is used for micro scale analysis and accordingly the analysis is made as a result of the electron beams interaction with the sample. SEM measurement equipment is electron source, gaps used for the control of the electron beam, condenser and magnetic lens systems. In the SEM system, measurements are made while both the electron source and the sample are under vacuum. Compared to optic microscopes, SEM could go deep from the material surface and provide better resolution measurements [49]. In addition to these, other superiorities are the ability to scan large surfaces and make measurements faster.




**Figure 3.7** SEM measurement device (Hitachi SU5000 model)

In this study, SEM measurements of the SnS thin film samples fabricated on SLG, Si, ITO and FTO substrates were examined by using Hitachi SU5000 model device (figure 3.7) in AYBU central laboratory. Before the measurement process, a thin layer of gold was coated on the samples surface to avoid charging problems.

### 3.3.4 Energy Dispersive X-ray Spectroscopy (EDS)

The elemental composition of the inspected material is specified using the energy dispersive X-ray spectroscopy (EDS) integrated into the SEM. Electron bombardment is performed on the material and material-electrons interaction occur. By virtue of these interactions, the X-ray is made uninterrupted on the subsurface of the material. The energy level and wavelengths that X-rays generate with each element on the material subsurface is different. The X-ray absorption of the element and the energy peak amplitude are analyzed by the EDS system software. In this way, the main elements are investigated swiftly.

EDS analysis of SnS thin films grown on SLG, Si, ITO and FTO substrates were done by Hitachi SU5000 model equipped with EDS facility at AYBU Central Laboratory.

### 3.3.5 Thickness Measurement

Thickness is a factor that has a significant effect on material properties and is used in characterization analysis. The thickness has a critical feature in structural, electrical and optical peculiarities of materials. In case the material is transparent, opaque, amorphous or crystalline is associated with the effect of thickness directly. The SnS thin films thickness analysis was obtained by using Veeco DEKTAK 6M profilometer as shown in figure 3.8. This device has a diamond tip and this tip scans vertically on the samples surface with reference to the substrate.



**Figure 3.8** Dektak 6M Profilometer

## 3.4 Electro-Optical Characterization of SnS Thin Films

### 3.4.1 Photoconductivity Measurements

Photoconductivity measurement was done with the Janis cryostat which was cooled using liquid nitrogen. These measurements were made under $3.75x10^{-6}$ Torr. For temperature dependent photoconductivity analysis of the films, the temperature range determined using liquid nitrogen was obtained. LakeShore 331 model temperature controller was utilized to control the temperature of the films. Temperature dependent measurement was done in the range of 100-340 K with 10 K measurement steps. Homogeneous illumination is provided on the sample with a 12-watt halogen lamp in the system. The illumination intensity of the halogen lamp is modified by Keithley 220 which varies between 50 and 90 mA with 10 mA measurement steps. The measuring ranges of the system are controlled by computer software entirely.

In this work, van der Pauv geometry which previously explained was used for photoconductivity measurements. The samples were placed into the cryostat and four-point connection was carried out using Cu wire. The system was delivered to the set vacuum via pump. By adding liquid nitrogen into the cryostat, the system was brought to desired temperature and then the measurement was started. The voltage was applied to the sample by Keithley 2400 and the resulting current values were recorded. At first, the measurements were done in a dark condition and then at different illumination intensities.

## 3.5 Optical Characterization of SnS Thin Films

### 3.5.1 Transmission Measurements

UV/Vis spectroscopy analysis is an ordinary hardly effective method used to measure optical transmission absorption coefficient values of materials. Using this method, the analysis of optical spectrum values such as transmittance and reflectance of the samples are investigated. Fundamentally, visible light (VIS) is sent to the surface of sample. Thereafter, the density of the photons transmitted from the sample is measured. Optical analysis of SnS thin films was performed with Perkin-Elmer

LAMBDA 45 UV/VIS/NIR spectrometer shown in figure 3.9. The analyzes of samples were made in the range of 300-1000 nm wavelengths. Background improvement was made in thin films using SLG, ITO and FTO substrates.



**Figure 3.9** Perkin-Elmer Lambda 45 Spectrometer

### 3.5.2 Current-Voltage (I-V) Measurements

The purpose of I-V measurement systems is to compose a current by applying voltage to the sample and thus to have information about electrical characterization of sample. The measurements made using I-V system is illustrated figure 3.10. After the probe connections were done between the sample and the measuring system, the samples were installed into the sample holder. In order to investigate 12-watt halogen lamp sensitivity of the samples, the measurement made under vacuum using different light intensities at the room temperature. A voltage difference is generated by applying voltage to the front and back surface of sample. The current corresponding to this voltage difference was measured with Keithley 2401 source meter. Analysis conditions and results were recorded by LabVIEW program.

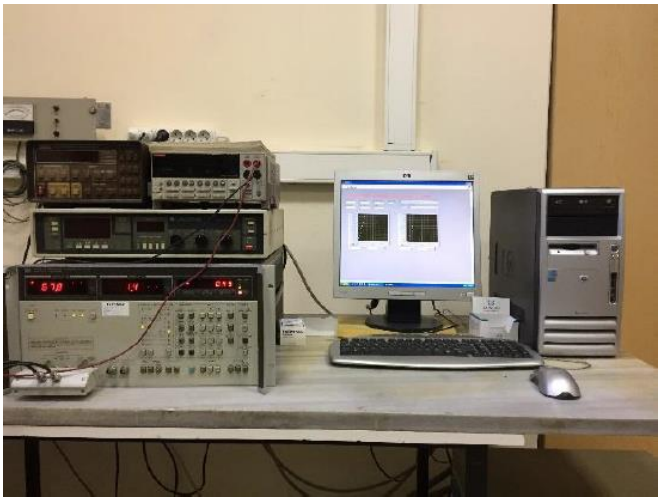


**Figure 3.10** I-V measurement system

## 3.6 Electrical Characterization of SnS Thin Films

### 3.6.1 Electrical Contacts

The front ohmic contacts of SnS thin films fabricated on n-type Si wafers and glass substrates were coated by a metallic evaporation system. A Cu shadow mask was utilized for the electrical measurements of the samples coated onto Si. This making process is done with copper masks in the form of a circular grid with a diameter of 1 mm. The masks with van der Pauv geometry were used in samples with deposited glass substrate. The electrical contact coating process was carried out using the thermal evaporation system shown in figure 3.11.



**Figure 3.11** Thermal evaporation system for metal coating

The backside of the n-type silicon wafer is coated with Ag metal using thermal evaporation system to form a contact surface. After coating, annealing at 450 ºC of was done in the Lindberg model furnace with continuous $N_2$ flow for ohmic Ag. The masks were attached to the samples were placed in the holder inside the thermal evaporation system. Indium was coated on front surface of the Si based thin films diode/p-n junction to constitute an ohmic contacts and investigation the diode behavior. In was used glass based thin films. Coating of metal contacts was carried out at room temperature and under $10^{-6}$ Torr. Pure elemental metals were put inside tungsten boat with particular operation. By applying voltage, the boat was heated and the metal was evaporated. The shutter was opened between source and the samples with the evaporation of the metal. When the metal coating was quitted, the shutter was closed and the voltage was reduced. To break the vacuum in the system was waited for a while and the samples were removed from the holder. After metal contact coating operation, post-heat treatment was adopted in order to provide metal diffusion. The samples were annealed in the furnace at 100 ºC for 30 minutes. Cu cables were connected to the fabricated contacts using Ag paste.

# CHAPTER 4

## RESULTS AND DISCUSSIONS

This section consists of two main parts. Firstly, structural, surface, and optical characterization of SnS thin film grown on different substrates are discussed. Secondly, electrical analysis of SnS thin film layer is presented. Finally, the optoelectronic properties of the films are explained by characterization results.

### 4.1 Characterization of SnS Thin Films Deposited on Different Substrates

In this section, the properties of SnS thin films were investigated by using different substrate materials. These substrates materials are soda lime glass (SLG), silicon (Si), indium tin oxide (ITO) and fluorine-doped tin oxide (FTO), respectively. SnS was deposited on the specified substrates materials via e-beam evaporation method. The effect of substrate materials type on structural, surface, and optical properties of SnS thin film was analyzed.

The selection of suitable substrate is crucial for thin film structures. In this study, SLG is the first choice because of its low cost. Si was preferred to research its effectiveness in photovoltaic applications. In addition, the most widely used ITO and FTO structures are samples of transparent conductive oxide (TCO). These n-type conductivity materials have been preferred to have good electrical conductivity in visible and infrared regions.

#### 4.1.1 Structural Properties of SnS Thin Films

With respect of the EDS results, the elemental composition of SnS thin films deposited on different substrates was determined. The weight and atomic proportions of the ingredient elements of the as grown films are shown in Table 4.1. Although SLG and Si stoichiometric ratios are border on each other, a Sn-rich film was obtained in ITO

and FTO. Stoichiometric differences emerged as the thickness control could not be fully performed during the deposition of the films.

**Table 4.1** The weight and atomic ratios of as-deposited SnS thin films

| Substrate | Sn (wt %) | S (wt %) | Sn (at %) | S (at %) |
|---|---|---|---|---|
| SLG | 78.53 | 21.47 | 49.71±14.23 | 50.29±12.17 |
| Si | 80.27 | 19.73 | 52.36±16.51 | 47.64±13.99 |
| ITO | 90.02 | 9.98 | 70.90±8.76 | 29.10±12.41 |
| FTO | 91.67 | 8.33 | 74.84±10.05 | 25.16±13.55 |

The crystallinity, phases and orientation of the film structure were analyzed for each deposition using the XRD technique. The effect of changing substrates on the film structure was investigated.

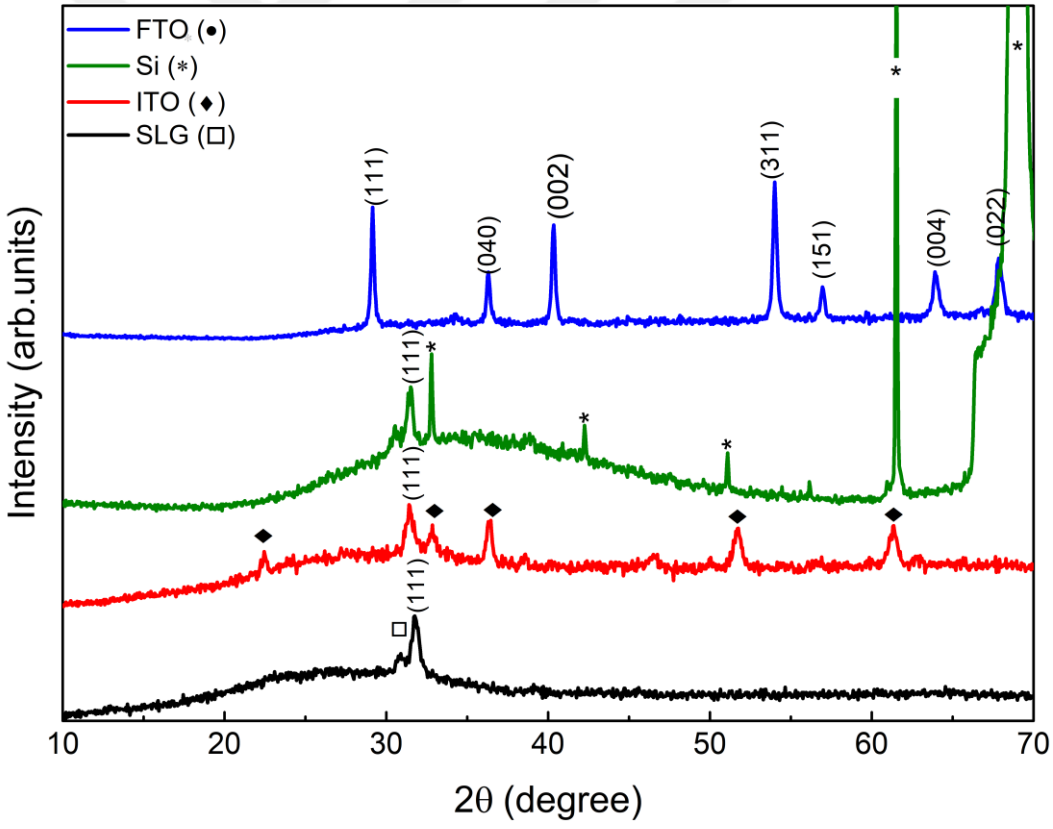



**Figure 4.1** XRD pattern of SnS thin films deposited on different substrates

In figure 4.1, XRD pattern from 2θ=10° to 70° for SnS thin films are given. According to XRD analysis, it was determined that the dominant structure (111) was the orthorhombic shape for substrates in SnS thin films by ICDD card no 89-2755 [50].

SnS phases for ITO and SLG substrates are shown in graph specially. SnS phases occurred in all substrates were indicated at the top which is in FTO peaks. The dominant orientation was detected (311) for FTO.

There can be multiple reasons for the dominant peak to shift. The first one is that the substrate are different and the lattice structure is formed in another type. Secondly, the formation of secondary phases ($SnS_2$, $Sn_2S_3$, $Sn_3S_4$) is common during the fabrication of SnS compound. On the other hand, the average thickness of the samples was calculated 200 nm. However, the distance from the place where the electron beam is located affects the thickness. Small thickness variations can be considered as a reason. Particle size (d) was determined according to XRD results using the Scherrer formula in equation 4.1.

$$d = \frac{K\,\lambda}{\beta \cos\theta} \qquad \textbf{(4.1)}$$

where K is Scherer constant, λ is wavelength of XRD system, β is full width at half maximum (FWHM) and θ is maximum peak angle [51]. The Cu Kα radiation of XRD system is 1.54 Å. Besides, the main peak orientation (111) was fit with the Gaussian function and the full width half maximum (FWHM) was obtained. The calculated values are given in table 4.2. The smallest grain size is found in SnS thin film grown on SLG.

**Table 4.2** XRD analysis results of SnS thin films deposited on different subsrates

| *Substrate Type* | *FWHM* | *Peak position (degree)* | *Crystallite Size (nm)* |
|---|---|---|---|
| SLG | 0.459±0.059 | 31.79±0.008 | 18.79±1.400 |
| ITO | 0.442±0.073 | 31.45±0.015 | 19.50±3.310 |
| FTO | 0.297±0.008 | 54.01±0.003 | 31.34±0.166 |
| Silicon | 0.395±0.048 | 31.47±0.010 | 21.82±2.720 |

### 4.1.2 Surface Properties of SnS Thin Films

The surface morphologies of SnS thin films were investigated with SEM. In figure 4.2, uppermost view SEM images of SnS thin film structure are given.

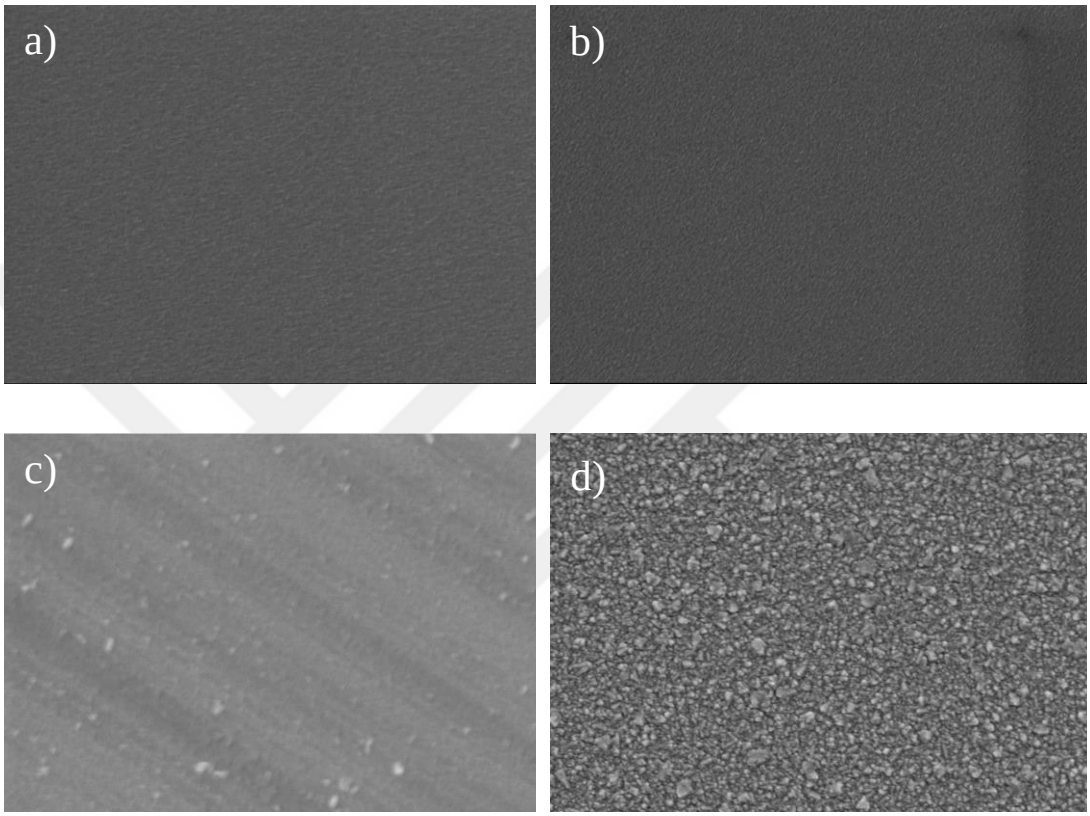



**Figure 4.2** SEM micrographs of SnS thin films deposited on a) SLG b) Si c) ITO and d) FTO for 2 μm scale

As can be seen in figure 4.2, the film morphology varies according to the substrate type. Different substrates have particular properties on the grain growth and microcrystalline structure of the deposited material. These differences directly affect the optoelectronic specification and performance of the film [52-53]. For all these reasons, the substrate and the material to be coated should be chemically compatible with each other and there should be no reaction between them. SnS thin film deposited on SLG and Si have a very smooth, compact and densely packed view. It is seen that randomly oriented pinholes are found in the film grown on ITO substrate. In the FTO sample, larger grains dispersed with less hole homogeneously. Increasing particle size

could result from a rough surface. Due to the greater nucleation area on the rough surfaces, the particles can collide and combine [54].

In addition to SEM analysis, AFM measurements were performed to susceptible analyze for surface morphology. According to AFM measurement, surface roughness values of SLG, Si, ITO and FTO samples are 1.8 nm, 6.4 nm, 5.9 nm and 2.1 nm, respectively. In figure 4.2, AFM analyzes for different substrates are given as two-dimensional (2D) and three-dimensional (3D) view.

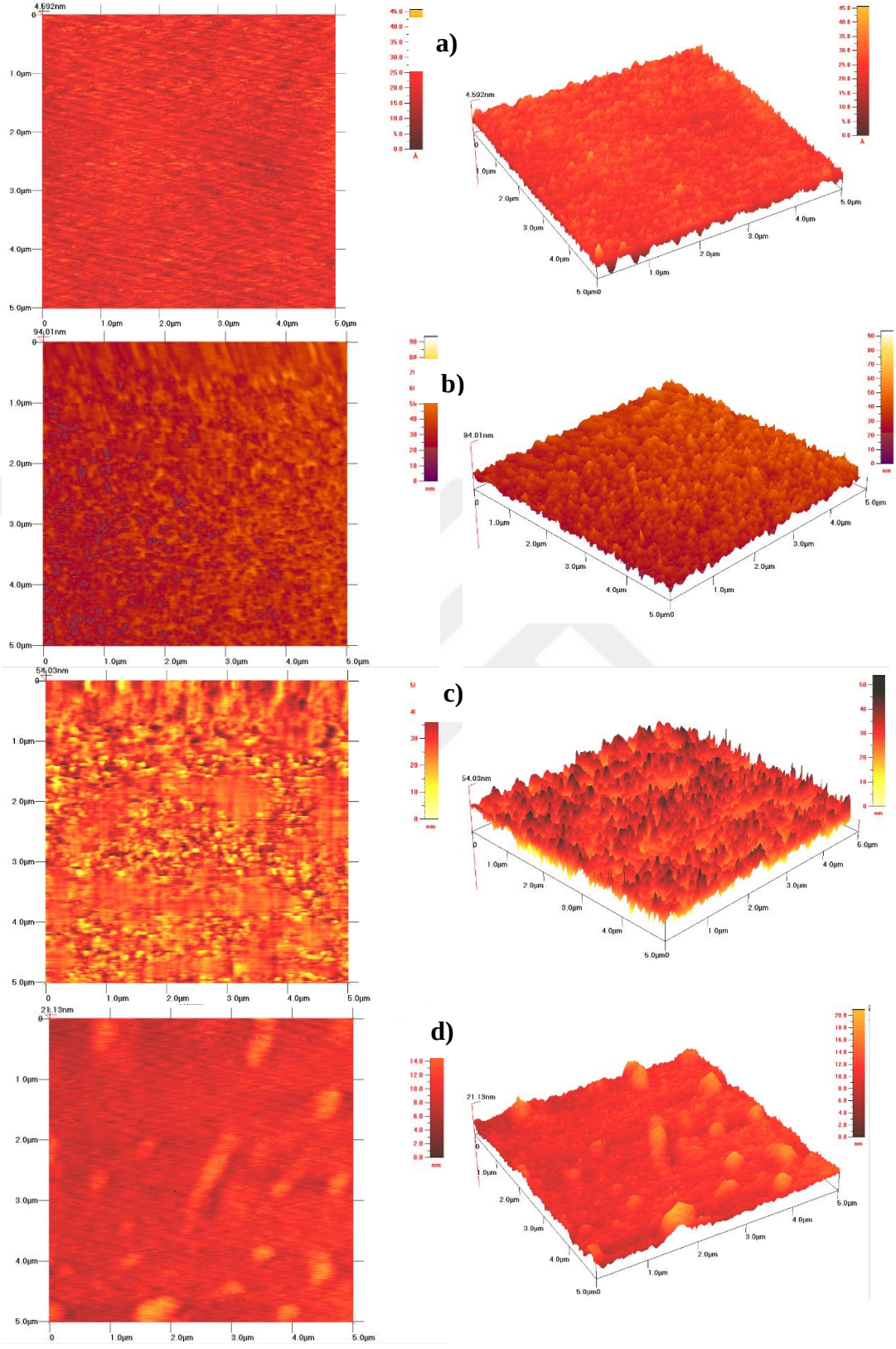



**Figure 4.3** The 2D (left) and 3D (right) 5 µm x 5 µm AFM images for thin film layer deposited on a) SLG, b) Si, c) ITO, d) FTO substrates

AFM images given in figure 4.3 were shown to give results consistent with SEM analysis and grain boundaries were clearly visible. The surface root mean square (RMS) values mentioned above are the conclusion of 3D images. RMS values are listed in Table 4.3.

**Table 4.3** List of RMS for SnS thin films deposited on different substrates

| Substrate | RMS |
|---|---|
| SLG | 1.8 nm |
| Si | 6.4 nm |
| ITO | 5.9 nm |
| FTO | 11.19 nm |

### 4.1.3 Optical Properties of SnS Thin Films

Optical characterization and optimization of the films are vital parameters for optoelectronic device applications. Optical properties of SnS thin films deposited on SLG, ITO and FTO were realized using LAMBDA 45 UV/NIS/NIR spectrometer device at room temperature between 300 nm to 1000 nm. The transmission plot was presented for each substrate and the $E_g$ values of the samples were calculated from Tauc plot by applying linear fitting.

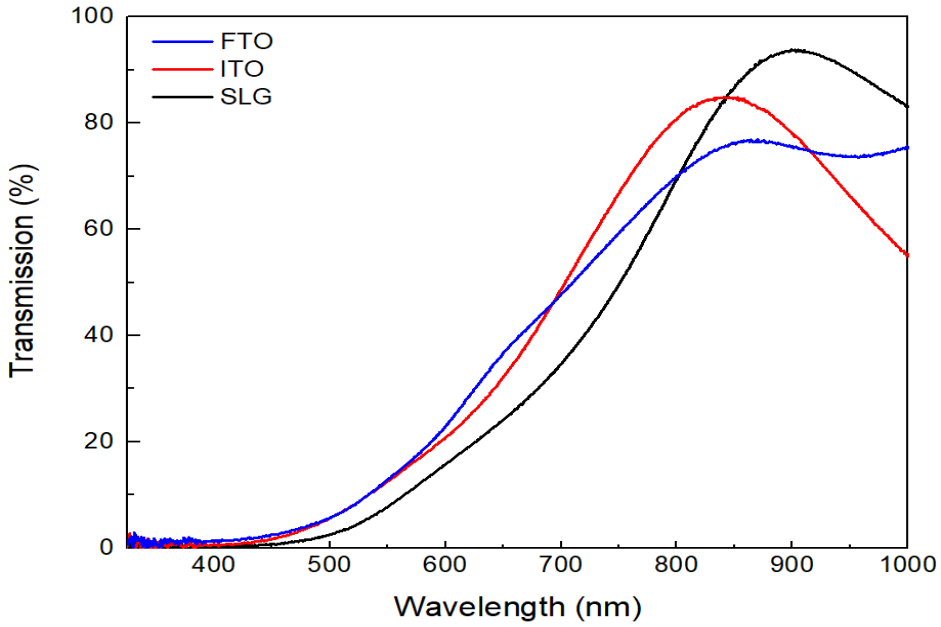



**Figure 4.4** Transmittance spectra SnS thin films for SLG, ITO and FTO substrates

As seen in figure 4.4, SnS thin films have high transmittance value in the visible light region. α for all films was calculated $10^4$ $cm^{-1}$. The transmission property directly affects the compliance of the substrate and SnS compound. Moreover, the transmission of substrate varies according to the wavelength value.

$E_g$ values of the samples were designated by $(\alpha h\nu)^2$ vs hν plot via extrapolating. The linearity of the given transmission or absorbance graphics represents that the films have a linear $E_g$. α was calculated by Lambert Beer Law using transmittance coefficient which is explained in Chapter 2.3.

The thickness of SnS structure was measured as 200 nm as a result of Dektak measurements. T is the transmission and this value varies from 300 nm to 1000 nm. Then, $E_g$ is calculated this formula 4.2.

$$(\alpha h\nu) = A\left(h\nu - E_g\right)^n \quad \textbf{(4.2)}$$

where hν is photon energy, α is absorption coefficient, $E_g$ is optical band gap and n is constant for optical transition mechanism which is ½ for direct band gap material. The extrapolation was made for α =0 condition. In figure 4.5, the linear fitting made according to the above formulas is given.

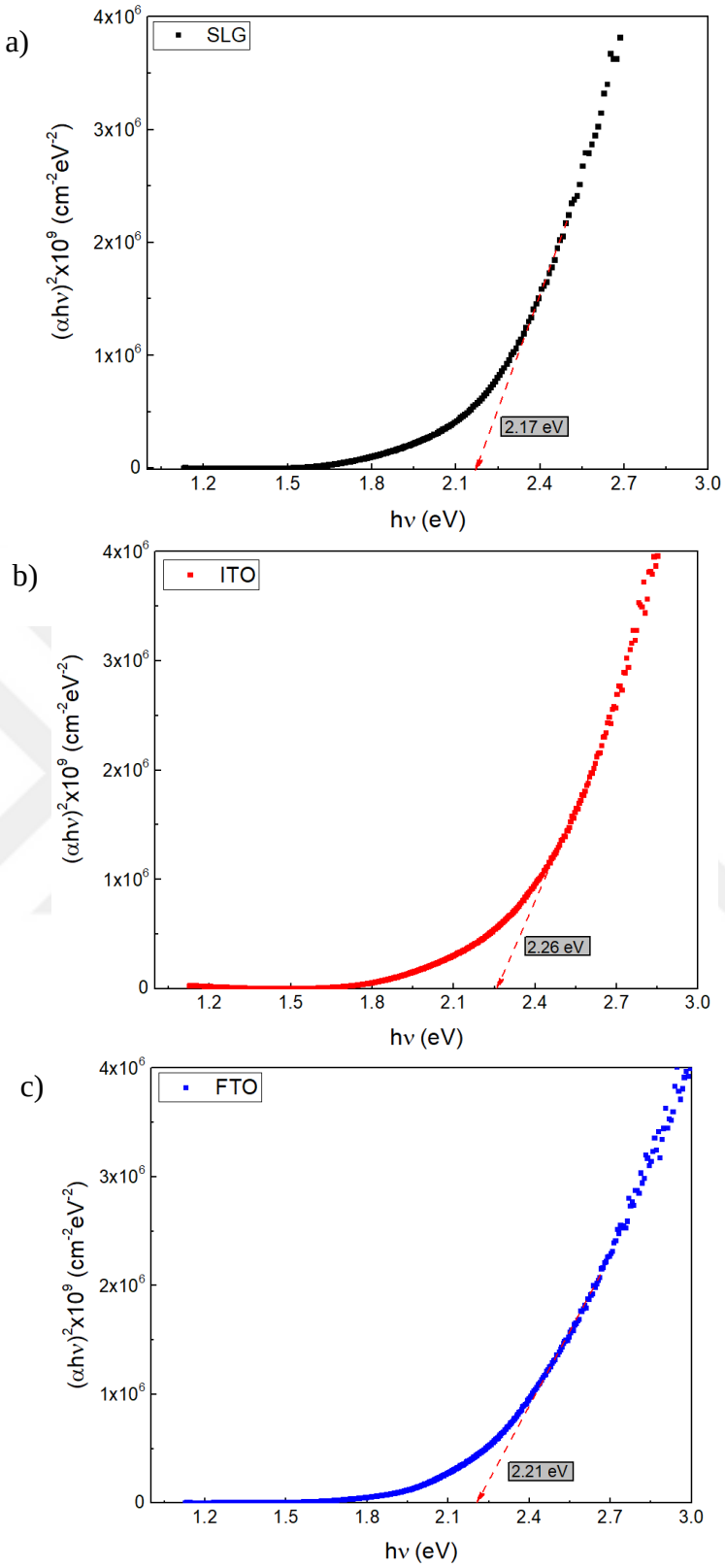



**Figure 4.5** Tauc plots of SnS thin films deposited on SLG, ITO and FTO substrates

As seen in figure 4.5, the band gap values of SnS thin films grown on SLG, ITO and FTO substrates as a result of linear fit process are 2.17 eV, 2.26 eV and 2.21 eV, respectively. In SEM and AFM result, the smoothest surface was found in SLG. The change in band gap value can be related to structural defects and imperfection of lattice in the film structure.

### 4.1.4 Electrical Properties of SnS Thin Films

SnS thin film samples fabricated with Van der Pauw geometry were utilized to analyze electrical properties. Van der Pauw geometry was obtained using the masks described in Chapter 2. Metal contacts were coated to form an ohmic contact with thermal evaporation method. In the temperature dependent $\sigma$ measurement, the test is done in dark condition firstly. Then, the I-V graph of the sample is expected to indication a linear behavior. The reason for this situation is the testing of the ohmic contact state of the metal and deposited material. After providing linearity in the dark condition, the illumination intensity is gradually increased. Depending on the reaction of the sample to the lighting, the measurements are conducted at different illumination intensity. Electrical characterization of SnS thin films was performed by temperature dependent $\sigma$ in both dark and illuminated conditions with intensity of 20, 35, 55, 85 and 115 mW/cm$^2$ as shown in figure 4.6.

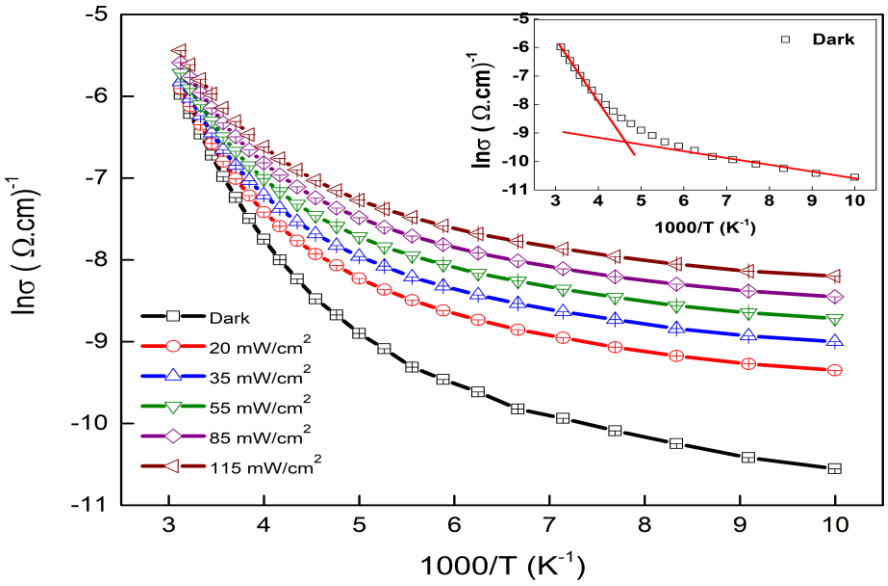



**Figure 4.6** Temperature dependent photoconductivity of SnS thin films and inset shows temperature range in the dark

As seen from figure 4.6, the $\sigma$ in the illumination condition is greater than the dark condition. The graph that gives SnS thin films photoconductivity shows the Arrhenius behavior. This behavior gives the change of temperature with light intensity and thus on conductivity. As in figure 4.6, data is in a straight line when the logarithmic of the conductivity and the reverse of the temperature are plotted. With this behavior, the determination of $E_a$ is used commonly [55]. In addition, the errors bars of the measurement are determined from the catalog as ±10 pA for current and ±1 μV for voltage, then included in the graph as seen in figure 4.6. The conductivity of the samples increased with rising illumination intensity. The photoconductivity measurements were made in the 100 to 340 K temperature range. The conductivity was investigated in the low temperature (100-250 K) and high temperature (260-320 K) range according to linearity of different temperature region as shown in figure 4.6 in. The graphic slope has larger values in the high temperature range and the $\sigma$ has increased with an exponential behavior. On the contrary, a decrease in slope was observed at low temperatures. The variation of $\sigma$ is determined using the equation 4.3:

$$\sigma = \sigma_0 exp\left(\frac{-E_a}{kT}\right) \quad \textbf{(4.3)}$$

where $\sigma_0$ is pre-exponential factor, $E_a$ is the activation energy. $E_a$ in the low and high temperature range are delivered in table 4.4.

**Table 4.4** Activation energy at different temperature ranges

| | Low temperature *Ea @100-250 K [meV]* | High temperature *Ea @260-320 K [meV]* |
|---|---|---|
| Dark | 26.7 | 175.8 |
| 25 mW/cm$^2$ | 18.8 | 131.7 |
| 35 mW/cm$^2$ | 17.4 | 113.1 |
| 55 mW/cm$^2$ | 16.9 | 105.9 |
| 85 mW/cm$^2$ | 16.3 | 100.5 |
| 115 mW/cm$^2$ | 15.9 | 96.6 |

It is seen that $E_a$ decreases with increasing light intensity in both temperatures. Moreover, the $E_a$ is greater in the high temperature than in low temperature. The calculated $E_a$ indicates the structural defects that occur during the processing of the films.

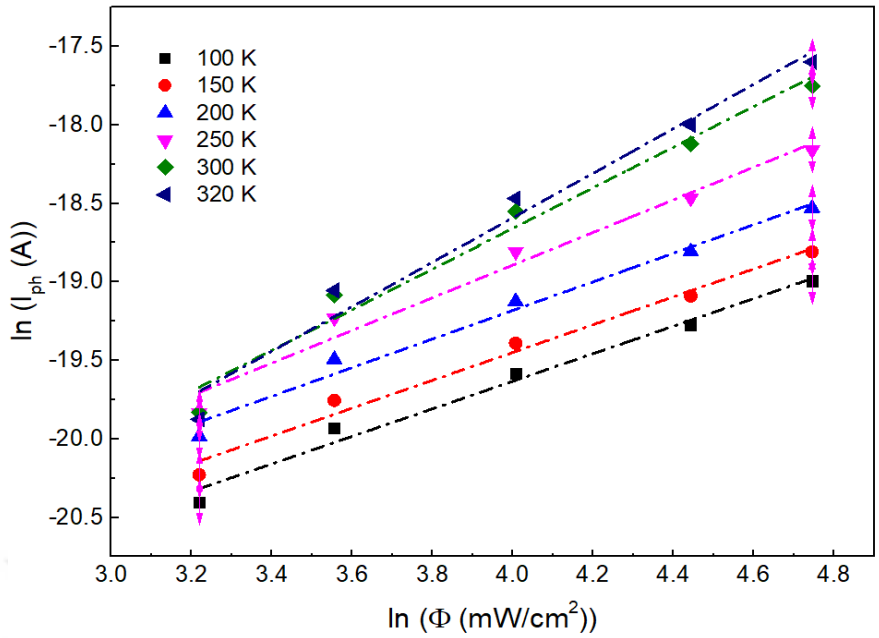



**Figure 4.7** The photocurrent- illumination intensity at different temperature

The correlation among photocurrent and illumination intensity at different ambient temperature were analyzed in figure 4.7. This analysis is vital to determine the recombination characteristic. The photocurrent and illumination intensity correlation can be expressed as $I_{ph} \propto \phi^n$. The power proportional constant was calculated for different ambient temperature. The value of n for 100, 150, 200, 250, 300 and 320 K is 3.21, 3.55, 4, 4,44 and 4.74, respectively. It is observed that the power proportional constant increased with raising the temperature. Transitions from bottom line to top line show stronger recombination of the free carriers on the film surface. The film at 300 K was determined to have long lasting lifetime and stronger recombination mechanism.

## 4.2 Device Characterization

Si-based devices are widely used to indicate the optoelectronic behavior of semiconductors. Si-wafers are mostly preferred in determining the diode structures of the thin film layers that are fabricated. In this section, main diode properties and dominant transmission mechanism of SnS thin film structure deposited on Si are investigated. It was investigated via temperature dependent I-V measurement and

temperature range from 220 K to 360 K. The device structure is In/p-SnS/n-Si/Ag as shown in figure 4.8.

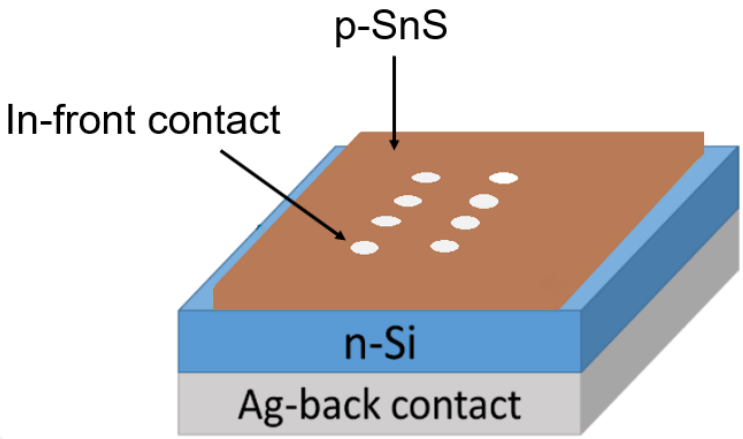



**Figure 4.8** The schematic diagram of In/p-SnS/n-Si/Ag device structure

The I-V properties of the heterojunction given schematic diagram is examined. Temperature dependent semi-logarithmic I-V graph is given in figure 4.9. As seen in the graph, forward bias current increased with an exponential behavior increasing forward voltage. Moreover, the saturation of the reverse forward current shown is a good behavior by the diode. The rectifying behavior of the I-V graph after the reverse bias current represents the depletion region at the SnS/Si interface. This structure was analyzed using the diode expression given below equation 4.4:

$$I = I_0 \left[ exp\left(\frac{q(V - IR_s)}{nkT}\right) - 1 \right] \quad \textbf{(4.4)}$$

V is the bias voltage, n is ideality factor and $I_0$ reverse saturation current defined as,

$$I_0 = AA^*T^2 exp\left(-\frac{q\phi_{b0}}{kT}\right) \quad \textbf{(4.5)}$$

where $\phi_{b0}$ is the zero-potential barrier, A is device active area, $A^*$ is the effective Richardson constant is 120 $A.cm^{-2}K^{-2}$ for n-type Si [56], [57].

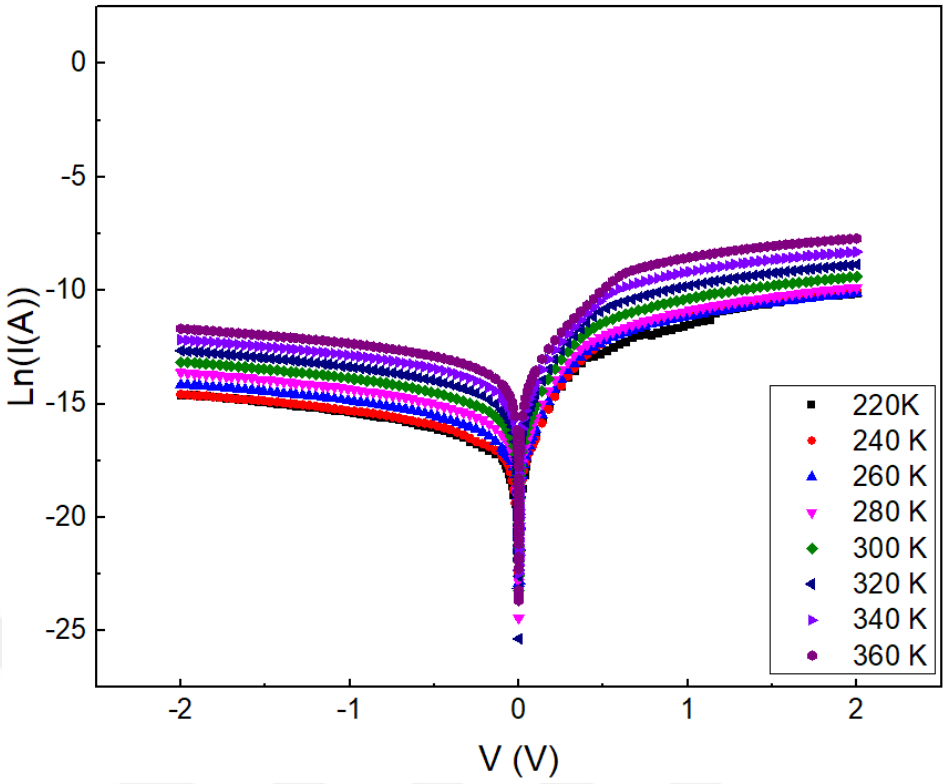



**Figure 4.9** Temperature dependent current-voltage graph of In/p-SnS/n-Si/Ag structure

Diode ideality factor, n, is inferred from equation 4.6:

$$\frac{1}{n} = \frac{kT}{q}\frac{d\left(In(I)\right)}{dV} \qquad \textbf{(4.6)}$$

The diode ideality factor should be equivalent to the value of the thermionic emission (TE) mechanism when the ideal contact is the dominant transport mechanism. n is decreases with increasing temperature and $\phi_{b0}$. The barrier height decreases due to surface homogeneity. All these parameters were estimated with the TE model.

From the I-V graph given above, n and $\phi_{b0}$ values were calculated depending on the absolute temperature. This calculation was done from the linear slope and axis intersections in the forward bias voltage region. $\phi_{b0}$ and n values are given in table 4.4. As seen in table 4.4, barrier potential has increased with temperature. When the temperature rises, potential carriers gain energy to contribute to the total current to exceed the barrier potential. The value of n decreased with the increase in temperature and ranged between 7.64 and 5.15. $R_s$ and $R_{sh}$ resistance are parasitic resistors of the device. $R_s$ and $R_{sh}$ deviates from forward and reverse linearity at saturated regions in

I-V graphs, respectively. It is observed that both resistances increase with temperature and decrease at high temperatures. According to the results shown in table 4.5, the barrier height value is in line with literature. In addition, the n value obtained greater than performed studies. Although $R_{sh}$ has approximately the same values, the $R_s$ is slightly higher than literature [58], [59], [60].

**Table 4.5** Results of temperature dependent I-V analysis of In/p-SnS/n-Si/Ag structure

| *Temperature (K)* | *Barrier Height* $\phi_{b0}$ *(eV)* | *Ideality Factor n* | *Series Resistance* $R_s$ *(Ω)* | *Shunt Resistance* $R_{sh} \times 10^5$ *(Ω)* |
|---|---|---|---|---|
| 220 K | 0.49 | 7.64 | 145 | 2.55 |
| 240 K | 0.54 | 5.97 | 602 | 7.24 |
| 260 K | 0.58 | 5.98 | 607 | 7.55 |
| 280 K | 0.62 | 5.88 | 606 | 6.86 |
| 300 K | 0.65 | 5.53 | 605 | 6.30 |
| 320 K | 0.69 | 5.30 | 593 | 5.45 |
| 340 K | 0.72 | 5.20 | 573 | 4.46 |
| 360 K | 0.75 | 5.15 | 555 | 1.64 |

The barrier height and n of the device in dark and different illumination intensity are given in table 4.6. I-V measurement was done to qualify the response of the device in the dark condition and different illumination intensity and shown in figure 4.10. In addition, $V_{oc}$, $I_{sc}$, FF and $\eta$ of the heterojunction were determined using I-V measurement as seen table 4.7. The calculated barrier height in the dark condition has a higher value compared to the different illumination intensity. This case is normal due to the low energy of carriers at dark condition. The rectifying factor increased with remaining the illumination intensity. At this stage, it is related to the energy of the carriers.

**Table 4.6** Results of I-V analysis of In/p-SnS/n-Si/Ag structure dark and under different illumination intensity

| *Condition* | *Barrier Height* $\phi_{b0}$ *(eV)* | *Ideality Factor n* |
|---|---|---|
| Dark | 0.653 | 5.53 |
| 20 mW/cm$^2$ | 0.551 | 6.73 |
| 35 mW/cm$^2$ | 0.542 | 6.80 |
| 55 mW/cm$^2$ | 0.536 | 6.87 |
| 85 mW/cm$^2$ | 0.532 | 6.91 |
| 115 mW/cm$^2$ | 0.528 | 6.92 |

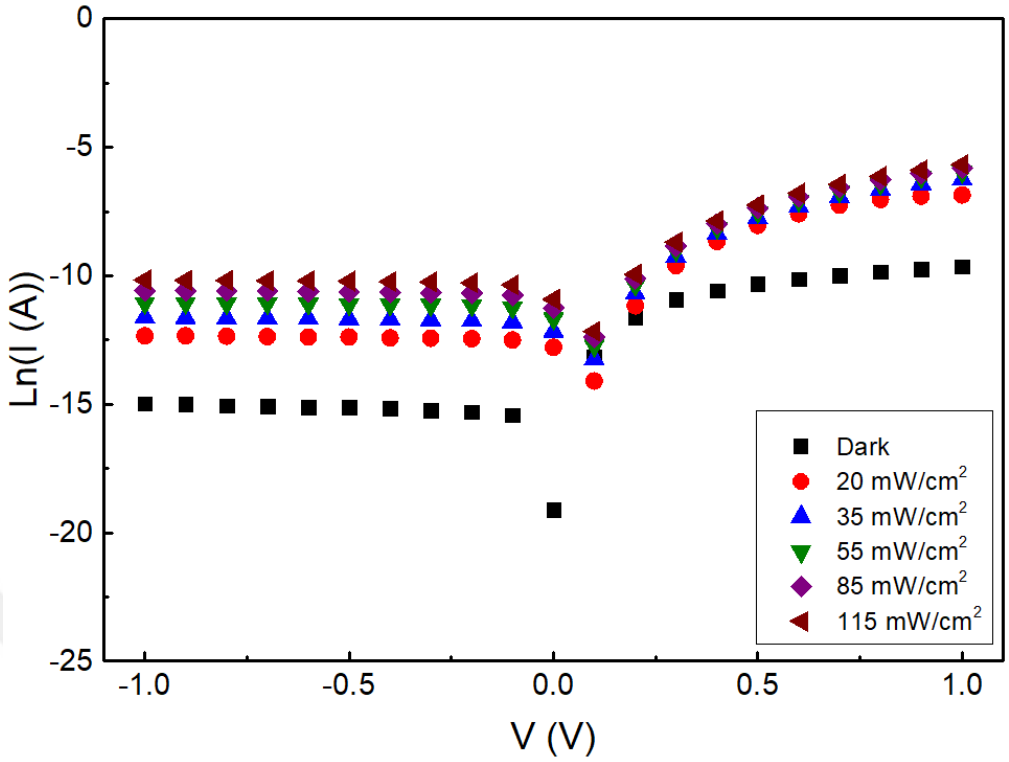



**Figure 4.10** Current-voltage graph of In/p-SnS/n-Si/Ag structure dark and under different illumination intensity at room temperature

The impact of the high series resistance can be seen in figure 4.10. The reason for this may be due to the effect of bulk layers and contact resistance. Because of the high $R_s$, increasing the recombination in photo carriers can be determined. This situation causes a decrease in solar cell efficiency.

**Table 4.7** The solar cell parameters of the p-SnS/n-Si structure

| Illumination intensity (mW/cm$^2$) | $I_{sc}$ (mA) | $V_{oc}$ (V) | FF | η (%) |
|---|---|---|---|---|
| 20 | 0.002807 | 0.122 | 0.27 | 0.24 |
| 35 | 0.005769 | 0.124 | 0.33 | 0.34 |
| 55 | 0.008569 | 0.127 | 0.33 | 0.33 |
| 85 | 0.012871 | 0.133 | 0.34 | 0.35 |
| 115 | 0.018233 | 0.123 | 0.36 | 0.39 |

The solar cell parameters of the sample are given in table 4.7. According to these results, it was determined that $R_s$ decreased FF. This situation affects the η directly.

# CHAPTER 5

## CONCLUSION

The aim of this study is to investigate the structural, surface and optical properties of SnS thin films deposited on different substrates. In the first part, the effect of different substrates such as SLG, ITO, FTO and silicon was analyzed. In the second part, which is another important part of the study, it is detailed electrical characterization of the SnS thin films fabricated on glass and Si to research optoelectronic properties. In addition, the characterization of the SnS thin film was done in broad spectrum. All of the different substrates were cleaned in accordance with chemical processes and then SnS thin films were fabricated using e-beam evaporation method. Before deposition, the substrates were sequentially stacked to the substrate's holder. In this case, the deposition was done under same conditions for each substrate and the thickness of samples were closed.

Elemental analysis of films was made by EDS measurement. SnS thin films grown on SLG and Si had $SnS = 1{:}1$ structure which is also stoichiometric. However, the films deposited on ITO and FTO were Sn-rich elemental composition. This is due to S element not being able to hold on these substrate configurations. The desired result has been achieved for glass and Si substrates. But stoichiometric control was not managed for ITO and FTO substrates.

Structural analysis of the films was made with XRD characterization. Structural analysis determined the crystal structures and orientations of the films. Transitions to secondary phases are difficult to control during the deposition of the SnS compound. Solely, phase transition control was achieved and secondary phase did not find in XRD results. It was concluded that SnS thin films have (111), (040) and (002) orientations and cubic structure in this study. However, the dominant orientation was determined (311) at $2\theta = 54.01°$ for FTO substrates. The main peak value for glass substrate was $2\theta = 31.79°$. This peak degree maintained the crystallization in all substrates. However, the main peak became evident at smaller angles with changing the substrates. While the main peak degree is 31.79 in glass, it is 31.47 in Si substrate. The

small change in the peak degree depends on the substrate type properties. On the other hand, the main peak showed the best crystallization in Si.

The surface analysis and composition of the deposited films were investigated with SEM and AFM. The surface roughness was low and flat surfaces were observed in the images in SnS structures grown on glass and Si substrates. For ITO and FTO substrates, the SnS compound was unevenly distributed on the surface. It was determined that these particles have large dimension. Accordingly, there was an increase in RMS value. Barely, cracks or holes were not found in the analyzed samples.

For optical characterization of SnS thin films, transmission spectroscopy was performed at wavelength ranging from 300 nm to 1000 nm. Depending on substrate type, a shift towards infrared region was detected in the transmission spectrum. Compared to ITO and FTO substrate, it is concluded that the glass substrate is more transparent. In SEM and AFM analysis, it was stated that crystallization was more homogeneous on glass. This case brought better optical density. It was educed that the substrate type affected the optical properties of thin film directly. The optical band gap values were calculated from Tauc graphs and varied between 2.17 eV and 2.26 eV.

Temperature dependent electrical characterization was impressed under different illumination intensity and dark condition. Temperature dependent photoconductivity measurement was carried out between 220 K and 360 K temperature range. In this temperature range, measurements were made under illumination at intensity of 20, 35, 55, 85, 115 $mW/cm^2$. It was calculated that the activation energy ranged from 26.7 to 15.9 meV for the low temperature range and 175.8 to 96.6 meV for high temperature. The SnS thin film samples were observed to be photosensitive feature over the entire temperature values. It was deduced that the samples had good rectifying factor in the transition from backward zone to forward zone.

Device characterization of the p-SnS/n-Si structure was measured by temperature dependent and different illumination intensity of I-V system. The In/p-SnS/n-Si/Ag heterostructure was fabricated. This structure has ohmic behavior and the device properties was detailed. Diode ideality factor is calculated greater than 5 in all temperature values. It has been determined that the $R_{sh}$ value reached maximum at 260 K. Depending on the $I_{sc}$ and $V_{oc}$ values, the efficiency was calculated as the lowest

0.24 and highest 0.39 value. The main diode parameters were calculated with the TE model. The $\phi_{b0}$ increased and the n of diode decreased with increase in temperature. By virtue of characterizations, In/p-SnS/n-Si/Ag structure shows photodiode feature.

# REFERENCES


[1] McEvoy, A., Castaner, L. and Markvart, T. Solar cells: materials, manufacture and operation: Academic Press, 2012.

[2] Richter, A., Hermle, M. and Glunz, S. W. Reassessment of the limiting efficiency for crystalline silicon solar cells. Ieee J Photovolt, 3 (4), 1184-1191. 2013.

[3] Yuan, M., Mitzi, D. B., Liu, W., Kellock, A. J., Chey, S. J. and Deline, V. R. Optimization of CIGS-based PV device through antimony doping. Chem Mater, 22 (2), 285-287. 2010.

[4] NREL, N. *Best Research-Cell Efficiency Chart*. US Department of Energy, https://www.nrel.gov/pv/cell-efficiency.html, 2020.

[5] Stavrinadis, A., Smith, J. M., Cattley, C. A., Cook, A. G., Grant, P. S. and Watt, A. A. SnS/PbS nanocrystal heterojunction photovoltaics. Nanotechnology, 21 (18), 185202. 2010.

[6] Sinsermsuksakul, P., Heo, J., Noh, W., Hock, A. S. and Gordon, R. G. Atomic layer deposition of tin monosulfide thin films. Adv Energy Mater, 1 (6), 1116-1125. 2011.

[7] Reddy, K. R., Reddy, N. K. and Miles, R. Photovoltaic properties of SnS based solar cells. Sol Energ Mat Sol C, 90 (18-19), 3041-3046. 2006.

[8] Solar, F. First solar press release, http://www.firstsolar.com/, 2016.

[9] Wesoff, E. First Solar hits Record 22.1% conversion efficiency for CdTe solar cell: Green Tech Media (PV Modules). 2016.

[10] Jackson, P., Wuerz, R., Hariskos, D., Lotter, E., Witte, W. and Powalla, M. Effects of heavy alkali elements in Cu (In, Ga) Se2 solar cells with efficiencies up to 22.6%. physica status solidi (RRL)–Rapid Research Letters, 10 (8), 583-586. 2016.

[11] Green, M. A., Dunlop, E. D., Levi, D. H., Hohl-Ebinger, J., Yoshita, M. and Ho-Baillie, A. W. Solar cell efficiency tables (Version 55). Prog Photovoltaics, 28 (1), 3-15. 2020.

[12] Woo, K., Kim, Y., Yang, W., Kim, K., Kim, I., Oh, Y., Kim, J. Y. and Moon, J. Band-gap-graded Cu 2 ZnSn (S 1-x, Se x) 4 solar cells fabricated by an ethanol-based, particulate precursor ink route. Sci Rep-Uk, 3, 30-69. 2013.

[13] Kafashan, H. X-ray diffraction line profile analysis of undoped and Se-doped SnS thin films using Scherrer's, Williamson–Hall and size–strain plot methods. J Electron Mater, 48 (2), 1294-1309. 2019.

[14] Hoffman, W. Ergebnisse der Strukturbestimmung komplexer. Sulfide. 1. Die Struktur von Zinnsulfid SnS and Teallit $PbSnS_2$. Zeit. Krist, 92, 161-173. 1935.

[15] El-Nahass, M., Zeyada, H., Aziz, M. and El-Ghamaz, N. Optical properties of thermally evaporated SnS thin films. Opt Mater, 20 (3), 159-170. 2002.

[16] Johnson, J., Jones, H., Latham, B., Parker, J., Engelken, R. and Barber, C. Optimization of photoconductivity in vacuum-evaporated tin sulfide thin films. Semicond Sci Tech, 14 (6), 501-589. 1999.

[17] Burton, L. A., Colombara, D., Abellon, R. D., Grozema, F. C., Peter, L. M., Savenije, T. J., Dennler, G. and Walsh, A. Synthesis, characterization, and electronic structure of single-crystal SnS, $Sn_2S_3$, and $SnS_2$. Chem Mater, 25 (24), 4908-4916. 2013.

[18] Dhanapandian, S., Manohari, A. G., Manoharan, C., Kumar, K. S. and Mahalingam, T. Optimization of spray deposition parameters for the formation of single-phase tin sulfide thin films. Mat Sci Semicon Proc, 18, 65-70. 2014.

[19] Sajeesh, T., Warrier, A. R., Kartha, C. S. and Vijayakumar, K. Optimization of parameters of chemical spray pyrolysis technique to get n and p-typelayers of SnS. Thin Solid Films, 518 (15), 4370-4374. 2010.

[20] Loferski, J. J. Theoretical considerations governing the choice of the optimum semiconductor for photovoltaic solar energy conversion. J Appl Phys, 27 (7), 777-784. 1956.

[21] Burton, L. A. and Walsh, A. Band alignment in SnS thin-film solar cells: Possible origin of the low conversion efficiency. Appl Phys Lett, 10 (13), 132111. 2013.

[22] Devika, M., Reddy, N. K., Patolsky, F. and Gunasekhar, K. Ohmic contacts to SnS films: Selection and estimation of thermal stability. J Appl Phys, 104 (12), 124503. 2008.

[23] Reddy, K., Devika, M. and Gunasekhar, K. Stable and low resistive zinc contacts for SnS based optoelectronic devices. Thin Solid Films, 558, 326-329. 2014.

[24] Patel, M. and Ray, A. Evaluation of back contact in spray deposited SnS thin film solar cells by impedance analysis. Acs Appl Mater Inter, 6 (13), 10099-10106. 2014.

[25] Nwankwo, S. N. Process. Post-Annealing Optimisation of SnS Thin Films with Alternative Buffer Layers. Published master's thesis, University of Northumbria. 2019.

[26] Steinmann, V., Chakraborty, R., Rekemeyer, P. H., Hartman, K., Brandt, R. E., Polizzotti, A., Yang, C., Moriarty, T., Gradečak, S. and Gordon, R. G. A two-step absorber deposition approach to overcome shunt losses in thin-film solar cells: using tin sulfide as a proof-of-concept material system. Acs Appl Mater Inter, 8 (34), 22664-22670. 2016.

[27] Moon, D. G., Rehan, S., Yeon, D. H., Lee, S. M., Park, S. J., Ahn, S. and Cho, Y. S. A review on binary metal sulfide heterojunction solar cells. Sol Energ Mat Sol C, 200, 109963. 2019.

[28] Abou-Ras, D., Kirchartz, T. and Rau, U. Advanced characterization techniques for thin film solar cells: John Wiley & Sons, 2016.

[29] Ghosh, B., Bhattacharjee, R., Banerjee, P. and Das, S. Structural and optoelectronic properties of vacuum evaporated SnS thin films annealed in argon ambient. Appl Surf Sci, 257 (8), 3670-3676. 2011.

[30] Sharon, M. and Basavaswaran, K. Photoelectrochemical behaviour of tin monosulphide. Solar cells, 25 (2), 97-107. 1988.

[31] Kawano, Y., Chantana, J. and Minemoto, T. Impact of growth temperature on the properties of SnS film prepared by thermal evaporation and its photovoltaic performance. Curr Appl Phys, 15 (8), 897-901. 2015.

[32] Reddy, V. R. M., Gedi, S., Park, C., Miles, R. and KT, R. R. Development of sulphurized SnS thin film solar cells. Curr Appl Phys, 15 (5), 588-598. 2015.

[33] Baby, B. H. and Mohan, D. B. The effect of in-situ and post deposition annealing towards the structural optimization studies of RF sputtered SnS and $Sn_2S_3$ thin films for solar cell application. Sol Energy, 189, 207-218. 2019.

[34] Roblin, P. and Rohdin, H. High-speed heterostructure devices: from device concepts to circuit modeling: Cambridge university press, 2002.

[35] Fukuda M. Optical semiconductor devices: John Wiley & Sons, 1999.

[36] Schroder, D. K. Semiconductor material and device characterization: John Wiley & Sons. 2015.

[37] Cardona, M. and Peter, Y. Y. Fundamentals of semiconductors: Springer, 2005.

[38] Streetman, B. G. and Banerjee, S. Solid state electronic devices: Prentice hall Englewood Cliffs, NJ, 1995.

[39] Sharma, B. L. and Purohit, R. K. Semiconductor heterojunctions: Elsevier, 2015.

[40] Kasap, S. O. Principles of electronic materials and devices: Tata McGraw-Hill, 2006.

[41] Qi, B. and Wang, J. Fill factor in organic solar cells. Phys Chem Chem Phys, 15 (23), 8972-8982. 2013.

[42] Chen, C. J. Physics of solar energy: John Wiley & Sons, 2011.

[43] Green, M. A. Solar cell fill factors: General graph and empirical expressions. SSEle, 24 (8), 788-789. 1981.

[44] Bube, R. H. Photoelectronic properties of semiconductors: Cambridge University Press, 1992.

[45] Çolakoğlu, T. The effects of post-annealing process on the physical properties of silver-indium-selenium ternary semiconductor thin films deposited by electron beam technique. Published Ph.D. thesis, Middle East Technical University, 2009.

[46] Demir, M. Structural, Optical and Electrical Characterization of Cdsexte1-X Thin Films. Published Master's thesis, Middle East Technical University, 2020.

[47] Mattox, D. M. Film Formation, Adhesion, Surface Preparation and Contamination Control, Handbook of physical vapor deposition (PVD) processing. Noyes publications, Westwood, New Jersey, USA, 1998.

[48] Cullity, B. D. Answers to problems: elements of X-ray diffraction. Addison-Wesley Publishing Company, 1978.

[49] Morita, S., Giessibl, F. J., Meyer, E. and Wiesendanger, R. Noncontact Atomic Force Microscopy: Volume 3. Springer, 2015.

[50] Devika, M., Reddy, N. K., Ramesh, K., Sumana, H., Gunasekhar, K., Gopal, E. and Reddy, K. R. The effect of substrate surface on the physical properties of SnS films. Semicond Sci Tech, 21, 10, 1495. 2006.

[51] Barrett, C. S., CS, B. and TB, M. Structure of metals. Crystallographic methods, principles and data, 1980.

[52] Reddy, V. R. M., Gedi, S., Pejjai, B., Kotte, T. R. R., Zoppi, G. and Park, C., Influence of different substrates on the properties of sulfurized SnS films. Sci Adv Mater, 8 (1), 247-251. 2016.

[53] Basak, A., Hati, A., Mondal, A., Singh, U. P. and Taheruddin, S. Effect of substrate on the structural, optical and electrical properties of SnS thin films grown by thermal evaporation method. Thin Solid Films, 645, 97-101. 2018.

[54] Holbrough, J., Campbell, J., Meldrum, F. and Christenson, H. Topographical control of crystal nucleation. Cryst Growth Des, 12 (2), 750-755. 2012.

[55] Ramesh, S., Yahaya, A. and Arof, A. Dielectric behaviour of PVC-based polymer electrolytes. Solid State Ionics, 152, 291-294. 2002.

[56] Andrews, J. and Lepselter, M. Reverse current-voltage characteristics of metal-silicide Schottky diodes. Solid State Electron, 13 (7), 1011-1023. 1970.

[57] Schubert, B. A., Marsen, B., Cinque, S., Unold, T., Klenk, R., Schorr, S. and Schock, H. W. $Cu_2ZnSnS_4$ thin film solar cells by fast coevaporation. Progress in Photovoltaics: Research and Applications, 19 (1), 93-96. 2011.

[58] Patel, M., Kim, H.-S. and Kim, J. Wafer-scale production of vertical SnS multilayers for high-performing photoelectric devices. Nanoscale, 9 (41), 15804-15812. 2017.

[59] Patel, M., Kim, J. and Kim, Y. K. Growth of Large-Area SnS Films with Oriented 2D SnS Layers for Energy-Efficient Broadband Optoelectronics. Adv Funct Mater, 28 (40), 1804737. 2018.

[60] Nandanapalli, K. R., Mudusu, D. and Reddy, G. K. Low-cost and nontoxic highly rectifying diodes using p-type tin monosulfide (SnS) thin films and Ti/Au binary contacts. Mat Sci Semicon Proc, 100, 192-199. 2019.

# CURRICULUM VITAE



## PERSONAL INFORMATION


**Name Surname** **:** Ceren YILDIRIM

**Date of Birth** **:** 11/01/1993

**E-mail** **:** cerennyldrmm@gmail.com


## EDUCATION

**Bachelor** **:** Erciyes University / Kayseri (3.26/4.00)

**Master** **:** Ankara Yıldırım Beyazıt University (2018-continued)

## WORK EXPERIENCE

**Trainee** **:** Xlim: Research Institute (France) (2020 January-April)

**Tübitak Scholar** **:** Ankara Yıldırım Beyazıt University (2019 September- 2020 January)

## TOPICS OF INTEREST

- Thin Film Solar Cells
- Perovskite Solar Cells

## CONFERENCE PROCEEDING

1. **C. Yildirim**, O. Surucu, M. Terlemezoglu, H. H. Gullu, A. Yildiz, "Characterization and Diode Application of SnS Thin Films for Si-based Photovoltaic Devices", The 5$^{th}$ International Conference on Engineering Sciences (Ankara, Turkey), 12223 (2019).

2. A. Atılgan, A. Atlı, **C. Yildirim,** A. Yıldız, "The Aging Time of Ionic Liquid and Paste Dependent Performance of DSSCs", The 5$^{th}$ International Conference on Engineering Sciences (Ankara, Turkey), 12125 (2019).

3. **Ceren Yıldırım**, Gamze Genç, M. Serdar Genç, Mustafa Soylak, "The Effect of Ice Accretion on The Wind Turbine Airfoil", International Symposium on Sustainable Aviation (İstanbul, Turkey), 2016.

**PROJECTS**

- Tübitak-1002, Scholar, "Fabrication of carbon-based perovskite solar cells", 2019.
- BAP- 5486, Researcher, "Boşluk İletim Tabakasız Tamamen Basılabilir Karbon Tabanlı Perovskite Güneş Pillerinin Üretilmesi", 2019.